

# THE COS-HALOS SURVEY: AN EMPIRICAL DESCRIPTION OF METAL-LINE ABSORPTION IN THE LOW-REDSHIFT CIRCUMGALACTIC MEDIUM

JESSICA K. WERK<sup>1</sup>, J. XAVIER PROCHASKA<sup>1</sup>, CHRISTOPHER THOM<sup>2</sup>, JASON TUMLINSON<sup>2</sup>, TODD M. TRIPP<sup>3</sup>,  
 JOHN M. O’MEARA<sup>4</sup>, AND MOLLY S. PEEPLES<sup>5</sup>

<sup>1</sup> UCO/Lick Observatory, University of California, Santa Cruz, CA, USA; [jwerk@ucolick.org](mailto:jwerk@ucolick.org)

<sup>2</sup> Space Telescope Science Institute, 3700 San Martin Drive, Baltimore, MD, USA

<sup>3</sup> Department of Astronomy, University of Massachusetts, Amherst, MA, USA

<sup>4</sup> Department of Chemistry and Physics, Saint Michael’s College, Colchester, VT, USA

<sup>5</sup> Department of Physics and Astronomy, University of California, Los Angeles, CA, USA

Received 2012 September 12; accepted 2012 December 4; published 2013 January 24

## ABSTRACT

We present the equivalent width and column density measurements for low and intermediate ionization states of the circumgalactic medium (CGM) surrounding 44 low- $z$ ,  $L \approx L^*$  galaxies drawn from the COS-Halos survey. These measurements are derived from far-UV transitions observed in *HST*/COS and Keck/HIRES spectra of background quasars within an impact parameter  $R < 160$  kpc to the targeted galaxies. The data show significant metal-line absorption for 33 of the 44 galaxies, including quiescent systems, revealing the common occurrence of a cool ( $T \approx 10^4$ – $10^5$  K), metal-enriched CGM. The detection rates and column densities derived for these metal lines decrease with increasing impact parameter, a trend we interpret as a declining metal surface density profile for the CGM. A comparison of the relative column densities of adjacent ionization states indicates that the gas is predominantly ionized. The large surface density in metals demands a large reservoir of metals and gas in the cool CGM (very conservatively,  $M_{\text{CGM}}^{\text{cool}} > 10^9 M_{\odot}$ ), which likely traces a distinct density and/or temperature regime from the highly ionized CGM traced by  $\text{O}^{+5}$  absorption. The large dispersion in absorption strengths (including non-detections) suggests that the cool CGM traces a wide range of densities or a mix of local ionizing conditions. Lastly, the kinematics inferred from the metal-line profiles are consistent with the cool CGM being bound to the dark matter halos hosting the galaxies; this gas may serve as fuel for future star formation. Future work will leverage this data set to provide estimates on the mass, metallicity, dynamics, and origin of the cool CGM in low- $z$ ,  $L^*$  galaxies.

**Key words:** galaxies: formation – galaxies: halos – intergalactic medium – quasars: absorption lines

**Online-only material:** color figures, machine-readable tables

## 1. INTRODUCTION

Galaxies are traditionally discovered and characterized by the emission from their stellar components. The majority of a galaxy’s stars are localized at one to a few tens of kiloparsecs from the center of their potential well, depending on the angular momentum and total mass of the system. Over the course of a Hubble time, the stellar system dominates the energetic output of the galaxy, drives its chemical enrichment, and ultimately defines its standing in the pantheon of modern galaxies.

Between the stars, at least in star-forming (SF) galaxies, lies a diffuse medium of gas, dust, and metals that comprises the interstellar medium (ISM). This predominantly neutral gas phase fuels star formation, receives energetic and kinetic feedback, and collects the material by-products from the stars that form and die. The ISM is a crucial component of young and growing galaxies. It further serves as a conduit for the light radiated by massive stars (and their explosions) in the form of H II regions and the photo-dissociation regions that surround them, and dust that converts UV/optical photons into infrared light.

It is now well recognized that a third, major baryonic component exists for galaxies in the form of a diffuse and ionized medium that extends to many tens, and even several hundreds of kiloparsecs from the galaxy (e.g., Morris et al. 1993; Lanzetta et al. 1995; Stocke et al. 1995; Chen et al. 1998; Tripp et al. 1998; Penton et al. 2002; Wakker & Savage 2009; Prochaska et al. 2011a). This reservoir, referred to as halo gas or the cir-

cumgalactic medium (CGM), permeates the dark matter halo and serves as both a supply of material for future star formation and as the gutter for gas, metals, and dust expelled from the central galaxy and/or its satellites and progenitors. Because it can mediate galaxy accretion and feedback, developing a complete picture of the CGM has clear and vital importance for understanding the formation of galaxies and their stellar systems. Furthermore, it is the fundamental intermediary of the baryonic cycle connecting galaxies to the intergalactic medium (IGM).

Although predicted many decades ago (Bahcall & Spitzer 1969), the discovery of the CGM awaited the pioneering efforts of J. Bergeron, who associated strong Mg II absorption in quasar spectra to a handful of  $L \approx L^*$  galaxies at close impact parameters to the sightlines (Bergeron 1986). The launch of the *Hubble Space Telescope* (*HST*) and successful operation of UV spectrographs have extended the study of the CGM to a multitude of far-UV transitions including the H I Lyman series (Lanzetta et al. 1995; Penton et al. 2002; Bowen et al. 2002). The first few generations of UV spectrographs (FOS, GHRS, and STIS), however, had only sufficient throughput for observations of the brightest active galactic nuclei in the sky. Consequently, while a few pioneering *HST* programs studied the gaseous envelopes of specific galaxies (e.g., Bowen et al. 1995), the majority of UV absorber surveys selected targets based on QSO properties such as brightness or redshift and not based on the properties of foreground galaxies (e.g., Shull et al. 1996; Penton et al. 2000; Davé & Tripp 2001; Tripp et al. 2008;

Thom & Chen 2008a, 2008b; Cooksey et al. 2010; Tilton et al. 2012). This has essentially limited studies of the low- $z$  CGM to small samples and/or galaxies at large impact parameters.

Our understanding of the CGM for  $L \approx L^*$  galaxies is especially limited. This limitation arises from the observation that a random QSO sightline will pass within 300 kpc of an  $L^*$  galaxy only once for every  $\Delta z = 0.25$  interval, and only one in four such sightlines will have a QSO pairing within 100 kpc separation (Tumlinson & Fang 2005). Most previous studies traced the inner CGM ( $R < 100$  kpc) using the Mg II doublet (e.g., Bowen et al. 1995; Barton & Cooke 2009; Chen et al. 2010; Bowen & Chelouche 2011). The results indicate a high incidence of strong Mg II absorption (70% covering fraction for  $R < 75$  kpc and  $W_r > 0.3 \text{ \AA}$ ), revealing the presence of a cool and metal-enriched CGM on these scales. Regarding far-UV transitions, only a handful of systems have been studied at Ly $\alpha$ , O<sup>+</sup>, or C<sup>+</sup> transitions with previous generations of UV spectrographs (Savage et al. 1998; Tripp & Savage 2000; Chen et al. 2001; Tripp et al. 2001; Prochaska et al. 2004, 2011a; Aracil et al. 2006; Stocke et al. 2006; Mulchaey & Chen 2009; Wakker & Savage 2009). These analyses have suggested a high incidence of H I gas around  $L^*$  galaxies and the occasional detection of highly ionized metals within a few hundred kiloparsecs. The samples have been too small, however, to properly assess the ionization state, to characterize its basic properties, or to explore trends with impact parameter, stellar mass, galaxy color, etc. It is worth noting that  $L^*$  galaxies are too rare to dominate the cosmic census of gas, dust, or metals. Analyses of their CGM, therefore, offer greater insight on the processes of galaxy formation than cosmology. Nevertheless, a detailed assessment may provide crucial insight into the formation of galaxies of all shapes and sizes.

With the explicit goal of assessing the multi-phase nature of halo gas in  $L \approx L^*$ , low-redshift galaxies, we have designed and executed a large program with the Cosmic Origins Spectrograph (COS; Froning & Green 2009; Green et al. 2012) on *HST*. Specifically, we targeted the halo gas of 38 galaxies drawn from the imaging data set of the Sloan Digital Sky Survey (SDSS) whose angular offsets from quasar sightlines and photometric redshifts implied impact parameters ( $R$ ) well inside their virial radii. The COS-Halos survey provides sensitive absorption-line measurements for a comprehensive suite of multi-phase ions from the spectra of 38  $z < 1$  QSOs lying behind the “target” galaxies. Our follow-up survey of these fields has revealed an additional 21 “bonus” galaxies included in our analysis that also lie at  $R < 160$  kpc to the sightlines. In aggregate, these data comprise a carefully selected statistically sampled map of the physical state and metallicity of the CGM for  $L \approx L^*$  galaxies.

In the first survey paper by COS-Halos, we examined the incidence of highly ionized, metal-enriched gas traced by the O<sup>+</sup> doublet (Tumlinson et al. 2011). To our surprise, the data revealed a very high incidence of strong O<sup>+</sup> absorption,  $N(\text{O}^+) > 10^{14.3} \text{ cm}^{-2}$ , in the CGM of SF  $L^*$  galaxies yet a relative lack of such ions in the CGM of non-SF galaxies. The mass in metals (and presumably baryons) of this highly ionized and possibly warm/hot ( $T > 10^5$  K) gas is substantial; we estimate a reservoir comparable to and likely far exceeding the mass of metals and gas in the ISM of  $L^*$  galaxies. The reason(s) for the absence of O<sup>+</sup> around red galaxies remain(s) an open question.

In companion papers, we have surveyed the incidence and distribution of H I gas of the CGM for these galaxies (Thom et al. 2012; J. Tumlinson et al., in preparation). The data reveal a very high incidence of strong H I Ly $\alpha$  absorption ( $W_r \gtrsim 1 \text{ \AA}$ ) at

nearly all impact parameters to the survey edge ( $R = 160$  kpc) for both SF and non-SF  $L^*$  galaxies. These results establish the presence of a cool-phase CGM around essentially all  $L^*$  galaxies. In this paper, we extend the analysis to the metal lines that may be associated with this H I gas. Such data are critical to assessing the ionization state, metallicity, and mass of the CGM.

This specific paper focuses on the absorption-line measurements for all ions except H I (J. Tumlinson et al., in preparation) and O<sup>+</sup> (Tumlinson et al. 2011). We present our Keck/HIRES spectroscopy for the first time and a comprehensive analysis of the COS spectra. We provide tables of the measured equivalent widths and column densities for all important transitions. We then examine empirical relations between the CGM and galaxy properties. In Section 2 we present the sample definition and the multi-wavelength data set; Section 3 details the metal-line identification and subsequent measurements of equivalent widths and column densities; Section 4 details the results of this empirical analysis, providing an examination of trends in CGM metal-line absorption with galaxy properties; Section 5 argues, based on these results, that the cool CGM ( $10^4 \text{ K} \lesssim T < 10^5 \text{ K}$ ) is predominantly ionized, metal-enriched, bound to the galaxy’s dark matter halo, and contains a significant reservoir of baryons for  $L^*$  galaxies; and finally, Section 6 offers a concise, bulleted list of our key results and conclusions.

Throughout this work we assume the five-year *Wilkinson Microwave Anisotropy Probe* cosmology with  $\Omega_\Lambda = 0.74$ ,  $\Omega_m = 0.26$ , and  $H_0 = 72 \text{ km s}^{-1} \text{ Mpc}^{-1}$  (Dunkley et al. 2009). For the purpose of this work, we define cool CGM gas in the temperature range  $10^4 \text{ K} \leq T < 10^5 \text{ K}$ , and warm CGM gas in the temperature range  $10^5 \text{ K} \leq T < 10^6 \text{ K}$ .

## 2. THE DATA

### 2.1. Sample Definition

The COS-Halos program targeted 38 galaxies with photometric redshifts  $z_{\text{phot}} \approx 0.15\text{--}0.4$  having a range of galaxy color ( $u - r$ ) and stellar mass  $M_* = 10^{9.5}\text{--}10^{11.5} M_\odot$ , and distributed at impact parameters  $R \approx 15\text{--}160$  kpc from a background, UV-bright quasar (see J. Tumlinson et al., in preparation for a complete description of the sample definition). The survey selection criteria implied no explicit biases regarding the galaxy inclination or local environment. Previous studies of Ly $\alpha$  absorption in galaxy halos have indicated that the CGM of  $L \approx L^*$  galaxies extends to at least 300 kpc (Rudie et al. 2012; Prochaska et al. 2011b). We emphasize that our survey probes the inner 160 kpc, and therefore may not probe the entire, metal-bearing CGM of  $L^*$  galaxies. Because of the occasional semi-catastrophic error in the photometric redshift, a small fraction of the galaxies have  $z \lesssim 0.1$  and correspondingly lower stellar mass and luminosity than expected. In the following, we restrict the study to galaxies with  $L > 0.1 L^*$  to isolate  $L \approx L^*$  galaxies, where we use the  $R$ -band absolute magnitude of  $-21.2$  for an  $L^*$  galaxy (Blanton et al. 2003). Future works will study the CGM of the fainter, dwarf galaxy population.

In the course of acquiring spectra for these targeted galaxies, we discovered an additional 21 galaxies at close impact parameters to the quasar and also with  $z < z_{\text{qso}}$  and  $L > 0.1 L^*$ . Although not our primary targets, these galaxies were selected without bias to CGM absorption and therefore are included in the following analyses, in identical fashion as the targeted sample. A full description of the galaxy spectra, photometry, and the inferred galaxy properties (e.g., SFR, stellar mass) is given in Werk et al. (2012). For convenience, Table 1 provides a

**Table 1**  
Galaxy Properties

Galaxy	$z$	$R$ (kpc)	$\log$ ( $M_*/M_\odot$ )	$L$ ( $L^*$ )	$u - r$	SFR ( $M_\odot \text{ yr}^{-1}$ )	Abund
J0226+0015_268_22	0.2274	78	10.80	0.51	> 2.08	< 0.09	****
J0401-0540_67_24	0.2197	83	10.14	0.37	1.25	1.14	8.55
J0803+4332_306_20	0.2535	77	11.30	1.63	> 2.81	< 0.21	****
J0910+1014_34_46	0.1427	112	10.61	0.60	1.51	14.12	8.52
J0910+1014_242_34	0.2641	135	11.43	2.16	> 2.44	< 0.30	****
J0914+2823_41_27	0.2443	101	9.81	0.37	1.24	2.83	8.62
J0925+4004_196_22	0.2475	83	11.29	1.48	> 2.58	< 0.57	****
J0928+6025_110_35	0.1540	91	10.78	0.52	2.55	< 0.04	****
J0935+0204_15_28	0.2623	110	11.00	0.79	> 2.23	< 0.10	****
J0943+0531_106_34	0.2284	121	10.79	0.74	2.24	4.52	8.89
J0943+0531_216_61	0.1431	149	10.95	0.72	2.82	< 0.03	****
J0943+0531_227_19	0.3530	92	9.59	0.24	> 1.17	0.47	8.49
J0950+4831_177_27	0.2119	91	11.20	1.44	2.74	< 0.30	****
J1009+0713_204_17	0.2278	60	9.85	0.28	1.39	4.58	8.32
J1009+0713_170_9	0.3557	44	10.23	0.29	0.93	3.04	8.73
J1016+4706_274_6	0.2520	23	10.21	0.23	1.48	0.64	8.62
J1016+4706_359_16	0.1661	44	10.47	0.44	1.80	1.37	8.83
J1112+3539_236_14	0.2467	53	10.31	0.52	1.42	5.68	8.48
J1133+0327_110_5	0.2367	18	11.22	1.94	2.38	< 0.29	****
J1133+0327_164_21	0.1545	55	10.07	0.19	1.29	1.83	8.55
J1157-0022_230_7	0.1638	19	10.84	0.55	2.48	< 0.09	****
J1220+3853_225_38	0.2737	154	10.75	0.66	> 2.10	< 0.13	****
J1233+4758_94_38	0.2221	132	10.76	0.70	2.13	4.38	8.94
J1233-0031_168_7	0.3185	32	10.53	0.37	1.38	3.42	8.42
J1241+5721_199_6	0.2053	20	10.16	0.20	1.42	4.32	8.78
J1241+5721_208_27	0.2178	93	10.04	0.20	1.53	1.06	8.66
J1245+3356_236_36	0.1925	112	9.83	0.20	1.27	1.05	8.58
J1322+4645_349_11	0.2142	37	10.78	0.58	2.02	0.62	8.91
J1330+2813_289_28	0.1924	87	10.32	0.24	> 2.50	1.99	8.61
J1342-0053_157_10	0.2270	35	10.93	1.08	1.56	6.04	9.05
J1342-0053_77_10	0.2013	32	10.49	0.25	> 2.45	< 0.30	****
J1419+4207_132_30	0.1792	88	10.61	0.55	1.75	11.36	8.63
J1435+3604_126_21	0.2623	83	10.37	0.33	> 2.22	5.56	8.44
J1435+3604_68_12	0.2024	39	11.09	1.37	1.78	18.96	8.81
J1437+5045_317_38	0.2460	143	10.14	0.46	0.98	4.29	8.48
J1445+3428_232_33	0.2176	113	10.40	0.29	1.92	2.60	8.69
J1514+3619_287_14	0.2122	47	9.68	0.18	> 1.49	1.96	8.68
J1550+4001_197_23	0.3125	102	11.33	1.78	2.02	< 0.16	****
J1550+4001_97_33	0.3218	150	10.90	0.82	> 1.96	7.42	8.62
J1555+3628_88_11	0.1893	34	10.52	0.54	1.43	4.18	8.74
J1617+0638_253_39	0.1526	101	11.52	2.65	2.73	< 0.23	****
J1619+3342_113_40	0.1414	97	10.10	0.19	1.67	1.33	8.49
J2257+1340_270_40	0.1768	116	10.90	0.67	2.80	< 0.06	****
J2345-0059_356_12	0.2539	46	10.83	0.80	1.80	< 0.14	****

**Notes.** Derived properties of target and bonus galaxies (see Werk et al. 2012 for details). Columns: (1) SDSS field identifier and galaxy identifier, where the first number is the position angle in degrees from the QSO and the second number is the projected separation in arcseconds (impact parameter) from the QSO. (2) Spectroscopic redshift as determined from LRIS and MagE data. (3) Projected separation between the galaxy and QSO in kpc, calculated in the rest frame of the galaxy. (4) Stellar mass from *kcorrect* (Blanton & Roweis 2007). (5) Galaxy luminosity in terms of  $L^*$ , where  $L^*$  is given by an  $R$ -band absolute magnitude of  $-21.12$  (Blanton et al. 2003). (6) SDSS  $u - r$  galaxy colors. (7) The Galaxy SFR, determined from a combination of emission-line spectroscopy and broadband photometry. (8) Oxygen abundance,  $12 + \log(\text{O}/\text{H})$ , determined for galaxies whose MagE and LRIS spectra showed strong emission lines, where the solar abundance is 8.69 (Asplund et al. 2005).

summary of the galaxies studied here and Figure 1 shows histograms of a few key properties. Throughout the paper, we identify each galaxy according to the quasar field and its angular offset from the quasar, e.g., galaxy J0042–1037\_358\_9 is located 9" from the quasar J004222.29–103743.8 oriented  $358^\circ$  east of north. Figure 2 shows the SDSS imaging and our Keck/LRIS spectrum of the representative galaxy J1233+4758 94\_38. Once we trim the sample to exclude galaxies with  $L < 0.1L^*$  and duplicate absorbers, defined as galaxies meeting all criteria outlined above with a more massive companion  $L^*$

galaxy at the same redshift (see discussion below), we are left with 44 galaxy absorbers in total.

Galaxies, owing to the processes of hierarchical structure formation, are known to cluster, form groups, and even merge with one another. For these reasons, "random"  $L^*$  galaxies often reside within a virialized galaxy cluster or group, and a smaller subset are currently experiencing a merger with another galaxy. In the former cases, standard treatment is to refer to the cluster (group) member as a satellite of the far more massive, underlying dark matter halo. At  $z \sim 0$ , models predict that tidal stripping

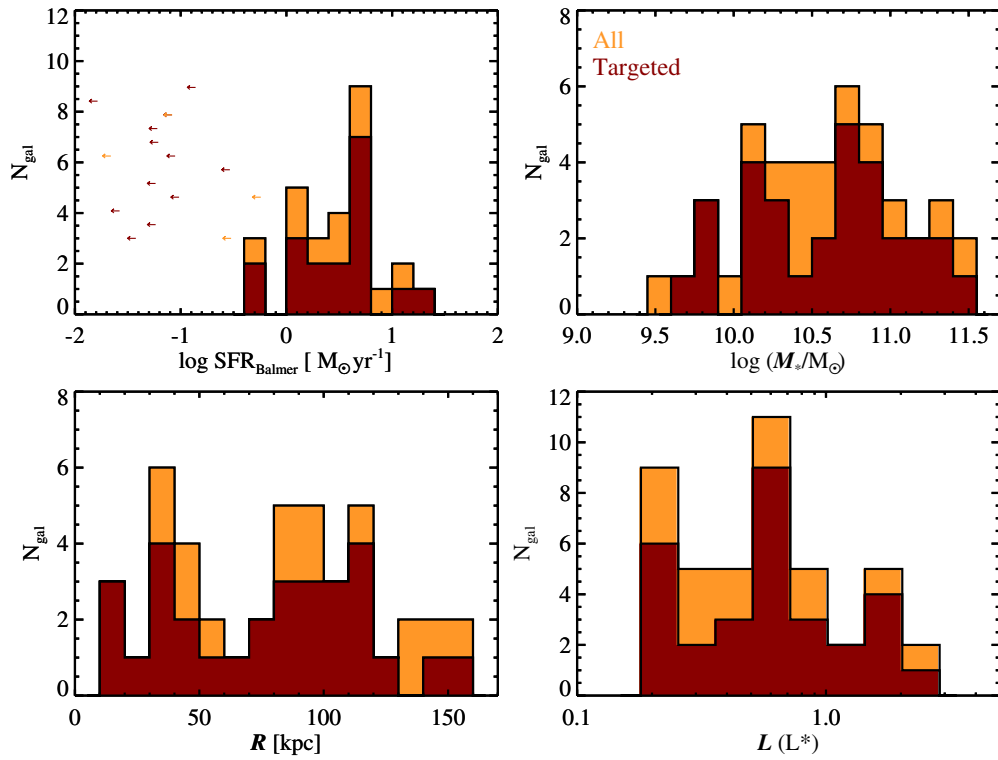


**Figure 1.** Histograms of the properties for the COS-Halos galaxies analyzed in this paper (see also Werk et al. 2012). At a given redshift, the sample comprises the closest, luminous ( $L > 0.1L^*$ ) galaxy with an impact parameter  $R < 160$  kpc of each sightline. The panels show the explicitly targeted galaxies (red) and the full sample (orange) which includes “bonus” galaxies discovered in the same quasar fields and which satisfy our sample criteria.  
(A color version of this figure is available in the online journal.)

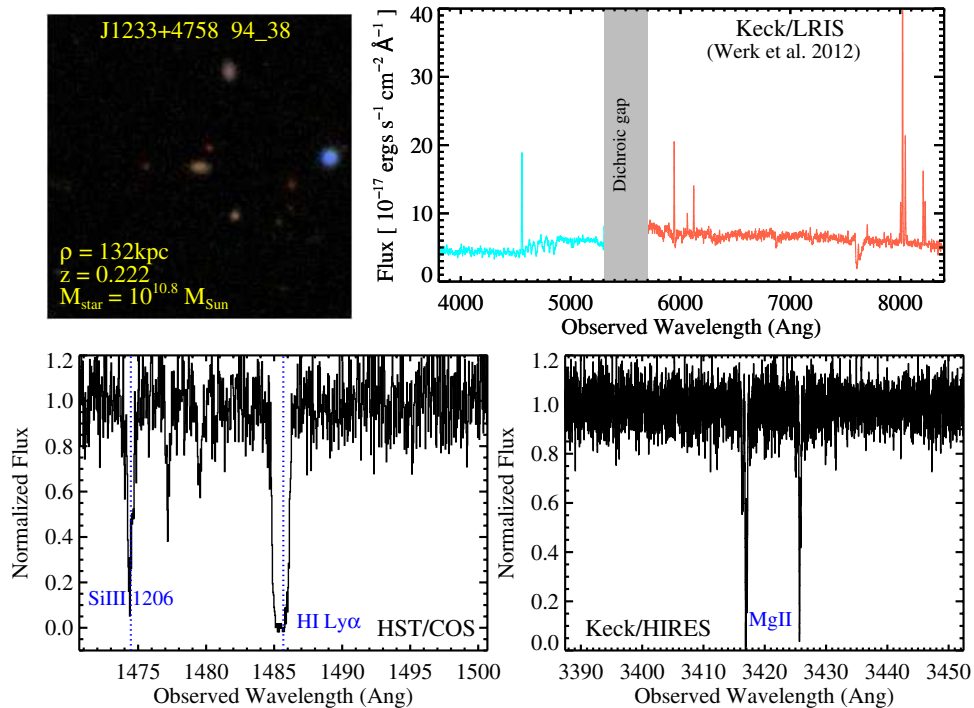


**Figure 2.** Montage of the SDSS image (upper left panel; 1/5 on a side) and Keck/LRIS spectrum (upper right) of an example target galaxy (J1233+4758\_94\_38), together with the *HST*/COS spectrum (lower left) zoomed-in on H I Ly $\alpha$  and the Keck/HIRES spectrum (lower right) zoomed-in on the Mg II doublet. These data are characteristic of the data set that has been gathered for nearly all of the galaxies in the sample.

(A color version of this figure is available in the online journal.)

significantly diminishes the size of the individual satellites’ halos (Okamoto & Habe 1999). By extension, we infer that a large fraction of the gas at  $R < 160$  kpc (pertaining to a galaxy’s CGM) would likely be distributed throughout the intracluster

or intragroup medium. In clusters, then, the localized intracluster or intragroup medium may dominate any observed absorption. This may be especially true for highly ionized species like  $O^{+5}$ .



For the COS-Halos sample, Werk et al. (2012) carefully considered the environments of our target and bonus samples, as assessed from previous analyses of SDSS spectroscopy and photometry (maxBCG cluster catalog; Koester et al. 2007), and reported that only five of the galaxies (within three QSO fields) are probable members of a massive group or galaxy cluster: J0928+6025: 110\_35 (0.766 Mpc projected from cluster center; 620 km s<sup>-1</sup> velocity offset), 129\_19 (0.731 Mpc projected from cluster center; 570 km s<sup>-1</sup> velocity offset), and 187\_15 (0.701 Mpc projected from cluster center; 700 km s<sup>-1</sup> velocity offset); J1016+4706: 359\_16 (0.573 Mpc projected from cluster center; 985 km s<sup>-1</sup> velocity offset); and J1514+3620: 287\_14 (19.3 Mpc from the cluster center; 1550 km s<sup>-1</sup> velocity offset). For reference, Koester et al. (2007) consider a galaxy to be a cluster member if the velocity offset is less than 2000 km s<sup>-1</sup>. In addition to those galaxies that match a maxBCG cluster, we find three galaxies in the QSO field J2257+1340 (270\_40, 238\_31, and 230\_25) that have confirmed spectroscopic redshifts  $z \sim 0.177$ , all of which are probable members of a previously unidentified group of galaxies. In our analysis, we treat these systems in identical fashion to the others.

While the complications related to group/cluster environments are predicted (and observed) to be a rare concern for our program, projected pairs of  $L \approx L^*$  galaxies are more common. Deep sky surveys reveal that the fraction of  $\sim L^*$  galaxies at  $z \sim 0.2$  that lie in close projected pairs is 2%–3% for  $R \leq 30$  kpc (e.g., Zepf & Koo 1989; Kartaltepe et al. 2007) and  $\sim 20\%$  for  $R \leq 100$  kpc (Lin et al. 2004). From our follow-up spectroscopy on the fields, there are seven cases where two or more  $L > 0.1L^*$  galaxies with a very similar spectroscopic redshift ( $\Delta z < 0.004$ ) lie within  $R = 160$  kpc of the same quasar sightline. This number includes two cases of galaxy cluster/groups identified in the previous paragraph (QSO sightlines J2257+1340 and J0928+6025). Based on SDSS galaxy catalogs and less-accurate photometric redshifts, at least 10 additional galaxies included in our study could have an  $L > 0.1L^*$  galaxy (in two cases, multiple galaxies) within a 300 kpc projected radius. In these cases, it is possible if not probable that the CGM of each galaxy contributes to the observed absorption. For example, the very high incidence of Ly $\alpha$  absorption from the CGM (e.g., Prochaska et al. 2011a; J. Tumlinson et al., in preparation) implies that any galaxy close to a quasar sightline will contribute H I absorption. In the case of galaxy pairs, assigning all of the observed absorption to a single galaxy would overestimate the CGM of that galaxy. It will be difficult if not impossible, however, to separate the contributions from each galaxy: the gas need not have identical velocity and line-blending further complicates the analysis.

For these reasons, we have taken the following approach to CGM analysis in fields where multiple galaxies lie close to the sightline and have velocity offset  $|\delta v| < 500$  km s<sup>-1</sup> based on spectroscopic redshifts. We associate all observed absorption with the CGM of the most massive galaxy (gauged by the stellar mass) with virial radius  $r_{\text{vir}} \geq R$  (see J. Tumlinson et al., in preparation). This approach is partly justified by the expectation that lower mass galaxies near the sightline will lie within the dark matter halo of the most massive galaxy. In this case, lower mass galaxies are considered satellites. In short, our procedure yields constraints on the CGM for a population of  $44 \approx L^*$  galaxies with a diverse set of environments. Future analysis will focus on the importance of environment for the nature of the CGM from such galaxies.

There are several systematic errors associated with this procedure. First, projection effects can occur; on occasion, placing the smaller galaxy within the halo of the larger will be incorrect because the two are truly well separated. Second, stellar mass is not a perfect proxy for dark matter halo mass. Third, interactions amongst galaxies and their satellites may be a crucial aspect of the formation and evolution of the CGM. It may be inappropriate or at least non-representative, to focus on the CGM of individual, isolated galaxies. Nevertheless, a proper treatment of modeling the CGM must take into account projection effects, the matching of stellar mass to dark matter halos, etc. Such analysis will be presented in a future paper of our own on this topic. This paper provides an empirical assessment of the CGM subject to the uncertainties described above.

## 2.2. COS Spectroscopy

J. Tumlinson et al. (in preparation) fully describe the acquisition, reduction, and calibration of the data from the Large Cycle 17 *HST* program (PID: 11598) known as COS-Halos whose COS spectroscopy provides all of the far-UV spectra analyzed here. For every sightline, these observations yielded a continuous spectrum spanning  $\lambda \approx 1150$ – $1800$  Å. The exposure times were chosen to achieve a signal-to-noise ratio (S/N) of 7–10 per resolution element (FWHM  $\approx 15$  km s<sup>-1</sup>) at  $\lambda \approx 1300$  Å. The analysis that follows was performed on the data binned by three native spectral “pixels” to a dispersion of  $\Delta\lambda \approx 0.0367$  Å.

Because the COS optics do not correct for the mid-frequency wave front errors arising from zonal irregularities in the *HST* primary, the true COS line-spread function (LSF) is not characterized by a single Gaussian. Instead, it is well described by a Gaussian convolved with a power law that extends to many tens of pixels beyond the line center (Ghavamian et al. 2009). These broad wings affect both the precision of our equivalent width measurements and complicate assessments of line saturation. We mediate these effects when we fit absorption lines (described in Section 3.3) by using the nearest wavelength grid point and convolving with the real LSF.

Although our coadding procedures properly preserve the Poisson counting statistics of the data, we find that we usually have enough counts in each pixel such that we can use standard propagation of error in the Gaussian regime. All of the spectra were continuum normalized with automated routines in  $\approx 20$  Å chunks centered on transitions of interest. These continuum models were visually inspected and manually adjusted as necessary. Figure 2 shows a representative slice of the COS spectra centered at the Ly $\alpha$  transition associated with the galaxy J1233+4758 94\_38. One also notes strong Si III  $\lambda 1206$  absorption consistent with this redshift.

## 2.3. HIRES Data

To supplement the far-UV spectra from *HST*/COS, we obtained Keck/HIRES echelle spectra for 35 quasars (Table 2). For galaxies at  $z > 0.1$ , these data provide coverage of the Mg II  $\lambda\lambda 2796, 2803$  doublet, an excellent diagnostic of cool ( $T \leq 10^4$  K), metal-enriched gas. Because these data were taken at substantially higher spectral resolution and (generally) higher S/N than the COS data, they also offer additional constraints on line saturation and the kinematics of the CGM.

The HIRES spectra were obtained over four runs spanning the nights of UT 2008 October 6, 2010 March 26, 2010 September 2, and 2012 April 12–13. On each night, the instrument was configured with the blue cross-disperser and collimator, i.e.,

**Table 2**  
Keck/HIRES Observations

Quasar	UT	$t_{\text{exp}}$ (s)	S/N <sup>a</sup>
J0033–0055	2008-10-06	3600	9.6
J0200–0845	2008-10-06	3000	6.5
J0226+0015	2008-10-06	3600	6.9
J0401–0540	2008-10-06	3600	9.3
J0803+4332	2012-04-12	2400	11.7
J0910+1014	2012-04-13	2400	6.9
J0914+2823	2012-04-13	2400	8.1
J0925+4004	2012-04-12	2400	5.4
J0928+6025	2010-03-26	3600	12.0
J0943+0531	2010-03-26	5400	11.8
J0950+4831	2012-04-12	2400	12.7
J1009+0713	2010-03-26	3600	9.3
J1016+4706	2012-04-13	2400	8.6
J1112+3539	2012-04-12	2400	7.2
J1133+0327	2012-04-13	2400	5.2
J1157–0022	2012-04-13	2400	8.2
J1233+4758	2012-04-12	2400	13.4
J1233–0031	2012-04-13	2400	9.9
J1241+5721	2012-04-12	2400	6.2
J1245+3356	2012-04-12	2400	13.1
J1322+4645	2010-03-26	3200	6.8
J1330+2813	2012-04-13	2400	4.5
J1342–0053	2012-04-12	2400	14.5
J1419+4207	2010-03-26	3200	11.4
J1435+3604	2012-04-13	2400	13.4
J1437+5045	2012-04-13	2400	6.4
J1445+3428	2012-04-12	2400	5.6
J1514+3619	2010-03-26	3200	6.9
J1550+4001	2012-04-13	2400	12.7
J1553+3548	2012-04-13	2400	15.3
J1555+3628	2012-04-12	2400	4.4
J1616+4154	2012-04-12	2400	14.3
J1619+3342	2010-09-02	3000	16.7
J2257+1340	2008-10-06	3600	13.5
J2345–0059	2008-10-06	2400	12.7

**Note.** <sup>a</sup> S/N per  $1.3 \text{ km s}^{-1}$  pixel at  $\lambda \approx 3400 \text{ \AA}$ .

HIRESb. We employed an echelle angle  $\text{ECH} = 0^\circ$  and a cross-disperser angle  $\text{XDANGL} \approx 1.0$  to give nearly continuous wavelength coverage from  $\lambda = 3050$  to  $5880 \text{ \AA}$  with  $\approx 20 \text{ \AA}$  gaps at  $\lambda \approx 3970$  and  $4965 \text{ \AA}$ , owing to the CCD mosaic configuration. We used the C1 decker for all observations giving a  $\text{FWHM} \approx 6 \text{ km s}^{-1}$  spectral resolution.<sup>6</sup> The data were reduced and calibrated using standard techniques with the HIREDUX<sup>7</sup> software package. The optimally coadded exposures (generally two per target) were continuum normalized with custom software, and a single combined spectrum sampled at  $\Delta v = 1.3 \text{ km s}^{-1}$  per pixel was generated for the absorption-line analysis. A portion of the Keck/HIRES spectrum for J1233+4758, centered at the Mg II doublet of the  $z = 0.2221$  94\_38 galaxy, is shown in Figure 2.

### 3. LINE MEASUREMENTS

This section discusses the metal-line measurements obtained from the *HST*/COS and Keck/HIRES quasar absorption-line

spectra. The analysis focuses solely on the absorption systems associated with spectroscopically confirmed galaxies foreground to our COS-Halos quasar sample. We further restrict the analysis to galaxies with impact parameters  $R \leq 160 \text{ kpc}$  and luminosity  $L > 0.1 L^*$ . In several fields, there are multiple galaxies located within  $160 \text{ kpc}$  and having systemic velocity offsets  $|\delta v| < 400 \text{ km s}^{-1}$  (e.g., J0928+6025). In Section 2.1, we discuss our approach to assigning properties of the CGM in such cases. For the following analysis, these issues only affect the zero point for the velocities reported.

We initiated the metal-line identifications by first searching for possible H I Lyman series absorption within  $\pm 600 \text{ km s}^{-1}$  of the galaxy spectroscopic redshift. J. Tumlinson et al. (in preparation) describe in detail that effort and the results. We then visually inspected the *HST*/COS and Keck/HIRES spectra at the expected locations of a large suite of far-UV transitions. If positive and consistent absorption was apparent, we defined a velocity interval to perform further analysis, attempting to maintain a constant interval for all metal-line transitions. This process also enabled a first-pass for flagging blends with Galactic absorption and/or coincident absorption from unrelated systems.

In parallel with this process, we generated velocity plots to further inspect the putative detections, refine the velocity intervals for analysis, and confirm probable blends. The plots of positive detections are given in Figure 3. Table 3 lists all of the transitions analyzed and the velocity interval for the analysis. For all line measurements, we have used atomic data from Morton (2003).

#### 3.1. Equivalent Widths

For all important transitions not severely compromised by a line-blend or sky emission, we measured the rest equivalent width  $W_r$  and estimated its uncertainty with a simple boxcar summation over the analysis interval. These intervals and the  $W_r$  measurements are given in Table 3. The errors reported are statistical only; one may adopt an additional  $\approx 20 \text{ m\AA}$  systematic error owing to uncertainty in continuum placement (of order 5%). We estimate this typical error by considering an absorption-line profile that spans  $100 \text{ km s}^{-1}$ , corresponding to  $430 \text{ m\AA}$  at  $1300 \text{ \AA}$  (observed), where 5% continuum placement error leaves us with an uncertainty of  $\approx 20 \text{ m\AA}$ . While  $20 \text{ m\AA}$  is a characteristic value for this uncertainty based on our data, one must bear in mind that the continuum placement uncertainty will more adversely affect the weakest, broadest, and shallowest absorption lines with a low central optical depth.

In cases where a line is significantly blended with another feature, we report the  $W_r$  measurement as an upper limit. We also provide upper limits ( $2\sigma$  statistical) for key transitions where the line is not detected at  $3\sigma$  statistical significance. For the majority of the COS spectra, this corresponds to a detection threshold of  $\approx 60 \text{ m\AA}$ . The important exceptions are the Si IV and C IV doublets, which lie at observed wavelengths  $\lambda > 1500 \text{ \AA}$ , where the sensitivity of COS is degraded.

#### 3.2. Apparent Optical Depth Method

At a spectral resolution of  $R \approx 20,000$ , the COS spectra will generally not resolve individual components of the metal-line profiles with characteristic line-widths  $b \leq 10 \text{ km s}^{-1}$ . Nevertheless, for weak absorption lines ( $W_r \lesssim 200 \text{ m\AA}$ ), the effects of line saturation should be modest.

Our primary evaluation of the column densities was derived using the apparent optical depth method (Savage & Sembach

<sup>6</sup> Unlike the COS spectra, the LSF for HIRES is well approximated by a single Gaussian.

<sup>7</sup> <http://www.ucolick.org/~xavier/HIREDUX/index.html>

**Table 3**  
Metal-line Measurements: Baseline Integration

Ion	$\lambda_{\text{rest}}$ (Å)	$[v_{\text{min}}, v_{\text{max}}]$ (km s <sup>-1</sup> )	$W_{\text{rest}}$ (mÅ)	$\log N$ (cm <sup>-2</sup> )	Flg	$\log N_{\text{Adopted}}$
J0226+0015_268_22 $z = 0.2274$ $R = 78$ kpc						
H I	949	[0, 250]	<73	<14.85	5	$14.25 \pm 0.03$
H I	1215	[0, 280]	$486 \pm 21$	$14.25 \pm 0.03$	1	
C II	1036	[-12, 332]	<34	<13.44	5	<13.44
C II	1334	[-12, 332]	<96	<13.69	5	
N I	1200	[-12, 332]	<56	<14.01	5	<14.01
N II	1083	[-12, 332]	<41	<13.59	5	<13.59
N V	1238	[-12, 332]	<64	<13.48	5	<13.48
O I	1302	[-12, 332]	<119	<14.29	5	<14.29
O VI	1031	[-12, 332]	<33	<13.41	5	<13.41
O VI	1037	[-12, 332]	<33	<13.72	5	
Mg II	2796	[-10, 201]	<60	<12.25	5	<12.25
Mg II	2803	[-10, 201]	<90	<12.71	5	
Si II	1190	[-12, 332]	<73	<13.44	5	<12.96
Si II	1193	[-12, 332]	<50	<12.96	5	
Si II	1260	[115, 332]	<200	<13.30	7	
Si II	1304	[-12, 332]	<103	<13.97	5	
Si III	1206	[-12, 332]	<57	<12.43	5	<12.43
Si IV	1393	[-12, 332]	<123	<13.14	5	<13.14
Si IV	1402	[15, 332]	<112	<13.43	5	
S II	1259	[55, 308]	<132	<14.84	5	<14.84
Fe III	1122	[156, 332]	<34	<13.74	5	<13.74

**Notes.** First line: SDSS field identifier and galaxy identifier, where the first number is the position angle in degrees from the QSO and the second number is the projected separation in arcseconds (impact parameter) from the QSO; Galaxy redshift, spectroscopically determined (Werk et al. 2012); and impact parameter in kpc. Columns: (1) metal ion name; (2) transition wavelength in Å; (3) velocity interval over which the transition was measured in km s<sup>-1</sup>; (4) equivalent width in mÅ; (5) log column density in cm<sup>-2</sup>; (6) transition flag: 1 = good, 3 = minorly blended, 5 = non-detection ( $2\sigma$  upper limit), 9 = saturated, and 11 = blended and saturated; (9) the adopted ionic column density, a weighted mean for ions with multiple detected transitions.

(This table is available in its entirety in a machine-readable form in the online journal. A portion is shown here for guidance regarding its form and content.)

1996), over the same interval used to measure the equivalent width. Additionally, we have derived column densities using the curve-of-growth technique, but they rarely give converged values because of the significant component structure of the observed absorption lines. While the curve-of-growth technique can be more accurate for a single component or profiles that are dominated by a single strong component, that condition does not often hold in these strong absorbers. These measurements and associated error estimates (statistical only) are presented in Table 3.

If the normalized flux of a given transition goes below 0.1 at any of the binned pixels, we have automatically set the column density to be a lower limit (saturated). Non-detections are listed as  $2\sigma$  (statistical) upper limits. The values for ions with multiple transitions were carefully inspected for consistency and signatures of line saturation. The measurements for many transitions are reported as lower limits due to line-saturation concerns. In cases with multiple measurements, we report the weighted mean in Table 3.

### 3.3. Profile Fitting

In addition to the AODM measurements of column densities, we fit Voigt profiles, where possible, to the detected absorption features in order to assess kinematic component structure and improve column density estimates of severely saturated lines. Additionally, profile fitting is essential for estimating the column densities of severely blended absorption lines, such as N III  $\lambda$ 989, which is often badly blended with Si II  $\lambda$ 989. The procedure used

to perform the fits and derive the column density  $N$ , Doppler  $b$ , and velocity offset  $v$  for each component is described in greater detail in J. Tumlinson et al. (in preparation). In short, it is an iterative fitting program that makes use of the MPFIT software<sup>8</sup> to optimize the fit and to generate errors near the best-fit point. The initial parameters, including the number of components, are set based on a by-eye examination of the data. Different transitions of the same ionic species are required to have the same component structure,<sup>9</sup> and are therefore fit simultaneously to give a single solution. However, we do not impose such requirements on the different ionization states of the same element.

We tabulate the results of this analysis in Table 4, and include the AODM-derived column density in the final column for comparison. The profiles that are fit to the data are shown along with the data in Figure 3. In the subsequent analysis, we use the AODM-derived total column densities in figures and throughout most of the analysis. As a conservative measure, we exclude badly blended lines from the analysis and treat saturated lines as lower limits. The total fit column densities are predominantly consistent with the AODM-derived columns, even in cases of complete blending (Si II  $\lambda$ 989 affects the total column density of N III  $\lambda$ 989 at the 1%–2% level), so this choice has no impact

<sup>8</sup> <http://cow.physics.wisc.edu/~craigm/idl/fitting.html>

<sup>9</sup> In this process, we include a nuisance parameter that allows for wavelength errors (i.e., a shift) between transitions. Owing to errors in the COS wavelength solution, these can be as large as 30 km s<sup>-1</sup> (e.g., J. Tumlinson et al., in preparation).

**Table 4**  
Metal-line Profile Fits and Final Column Densities

Ion	$v^a$ (km s <sup>-1</sup> )	$\sigma(v)$ (km s <sup>-1</sup> )	$b$ (km s <sup>-1</sup> )	$\sigma(b)$ (km s <sup>-1</sup> )	log $N$	$\sigma(N)$	log $N_{\text{AODM}}$
J0226+0015_268_22 $z = 0.2274$							
J0401-0540_67_24 $z = 0.2197$							
C III	-65.2	5.8	12.7	8.1	13.72	0.43	>14.00
	-13.9	6.3	25.1	7.5	13.97	0.15	
N III	-45.7	5.7	14.7	13.6	14.01	0.38	14.57 ± 0.05
	8.1	17.3	54.4	16.8	14.45	0.14	
O VI	-59.3	6.8	33.3	7.7	14.25	0.10	14.52 ± 0.02
	6.0	5.5	27.9	6.0	14.25	0.08	
Si III	-57.3	5.2	42.0	7.7	12.91	0.06	12.88 ± 0.06
J0803+4332_306_20 $z = 0.2535$							
C III	-36.8	3.6	17.1	6.2	13.55	0.13	13.66 ± 0.06
	13.6	4.0	10.5	7.6	13.29	0.23	
J0910+1014_34_46 $z = 0.1427$							
C IV	-97.2	1.8	20.7	2.6	14.16	0.05	14.10 ± 0.09
	-28.7	8.0	23.7	13.9	13.29	0.17	
O VI	-105.3	17.2	100.0	22.3	14.66	0.09	>14.56
Mg II	-87.2	0.5	7.0	0.6	12.83	0.05	>13.29
Si III	-109.5	3.8	23.3	6.7	13.42	0.15	>13.28
	-47.2	14.4	17.4	22.8	12.39	0.31	

**Notes.** First line: SDSS field identifier and galaxy identifier, where the first number is the position angle in degrees from the QSO and the second number is the projected separation in arcseconds (impact parameter) from the QSO; Galaxy redshift, spectroscopically determined (Werk et al. 2012). Columns: (1) metal ion name; (2) component velocity in km s<sup>-1</sup> and (3) associated error; (4) component Doppler width and (5) associated error; (6) log column density of the fitted component and (7) associated error; (8) the AODM column density, for reference. A few of the component Doppler parameter errors of especially weak absorption lines are given as -0.0, a red flag that the fits should not be trusted in those particular instances.

(This table is available in its entirety in a machine-readable form in the online journal. A portion is shown here for guidance regarding its form and content.)

on the results and trends that follow. The primary utility of the fits for this work is in a component analysis, which we touch on in Sections 4 and 5.

#### 4. RESULTS

In this section, we describe the principal results drawn from the equivalent width and column density measurements of the low and intermediate metal-line transitions associated with the CGM of  $L \approx L^*$  galaxies. In most of this analysis, we distinguish between SF galaxies and non-SF galaxies according to a strict cut in the observed specific star formation rate (sSFR). The SF galaxies (depicted with blue points) are required to have  $\text{sSFR} > 10^{-11} \text{ yr}^{-1}$ . All of the galaxies in the non-SF sample ( $\text{sSFR} < 10^{-11} \text{ yr}^{-1}$ ) have no measurable star formation as estimated from H $\alpha$  and [O II] emission lines (Table 1; Werk et al. 2012).

Unfortunately, the redshifts of our target galaxies generally place the C IV doublet beyond the wavelength coverage of the COS spectra. Furthermore, those systems with coverage of C IV frequently have poor data quality because of the lower sensitivity of COS beyond  $\approx 1500 \text{ \AA}$ . As such, we have only a handful of measurements, which may suggest a high covering fraction of C<sup>+</sup> for SF galaxies. While our data set does permit the analysis of Si IV for the majority of systems, the lower COS sensitivity at longer wavelengths implies that strong absorption ( $\gtrsim 200 \text{ m\AA}$ ) is required for a positive detection. We exclude these higher ionization state lines from this analysis (though they are tabulated) since there is little to be learned from them in this specific data set.

Because many of the sets of measurements include limits (upper and lower), we occasionally employ the ASURV software

package to perform statistical analysis (Feigelson & Nelson 1985). For the bivariate tests, we implicitly assume that the limits are random with respect to the galaxies. Given the range of impact parameters sampled and that the quasars were selected without any knowledge of the absorption, this method should hold. We also perform “standard” statistical tests by treating the limits as values and discuss whether this implies a conservative (or risky) assessment.

##### 4.1. Low Ions

As discussed in Thom et al. (2012) and J. Tumlinson et al. (in preparation), the COS-Halos sample almost uniformly exhibits strong H I absorption ( $W_{\text{Ly}\alpha} \gtrsim 1 \text{ \AA}$ ,  $N_{\text{H I}} \geq 10^{14} \text{ cm}^{-2}$ ). This indicates a substantial, cool gas phase for the CGM at  $R < 160 \text{ kpc}$  from  $L^*$  galaxies, independent of galaxy properties. If this medium is significantly enriched in heavy elements, then we may expect to detect at least a trace amount of dominant low ions (e.g., Si<sup>+</sup>, O<sup>0</sup>, Mg<sup>+</sup>). For the purposes of this work, we define “low ions” to be the first ion of each heavy element that has an ionization potential exceeding 1 Ryd. These should be the dominant ions in an optically thick gas where photons with  $h\nu > 1 \text{ Ryd}$  are preferentially absorbed by the surrounding hydrogen.

In Figure 4, we show the equivalent width and column density measurements for the three low ions with a sensitive and large sample of measurements: Mg<sup>+</sup>, Si<sup>+</sup>, and C<sup>+</sup>. These quantities are plotted against the physical impact parameter  $R$  from the quasar sightline to the galaxy. The SF and non-SF galaxies are denoted by color (blue and red, respectively) and the symbol size is proportional to the measured H I column density (scaled linearly from log  $N_{\text{H I}} = 13$  to 17).



Focusing first on the SF galaxies, which dominate the sample, each ion shows weaker absorption at larger  $R$  (i.e., lower equivalent widths and column densities). Similarly, the fraction of sightlines with non-detections increases with  $R$  (Tables 5 and 6). For example, the median equivalent width of C II  $\lambda 1036$  (Mg II  $\lambda 2796$ )  $\tilde{W}_{1036}$  ( $\tilde{W}_{2796}$ ) drops from 204(314) mÅ for  $R < 75$  kpc to 59(85) mÅ for  $R > 75$  kpc, while the median low ion column density drops from  $N(\text{C}^+) = 10^{14.4}$  to  $10^{14.0} \text{ cm}^{-2}$  for C and  $\tilde{N}(\text{Mg}^+) = 10^{13.3}$  to  $10^{12.3} \text{ cm}^{-2}$  for Mg. One draws similar results from estimates of the average values, although such analysis is complicated by the presence of both upper and lower limits. A two-sample log-rank test using the ASURV package on the  $W_{2796}$  or  $N(\text{Mg}^+)$  values<sup>10</sup> rules out the null hypothesis that the  $R < 75$  kpc and  $R > 75$  kpc subsets being drawn from the same population at 98% confidence.

One concludes, at high confidence, that the average surface density of low ions decreases with increasing impact parameter. This must reflect a decreasing total surface density, a decreasing metallicity, and/or an increasing ionization state with increasing  $R$ . Since it is likely that the H I column density also decreases with increasing impact parameter (J. Tumlinson et al., in preparation), an outwardly decreasing CGM metallicity gradient is the least likely to drive the main effect. Despite the decreasing column of low ion gas with increasing  $R$ , we report positive detections to at least 130 kpc and lack sufficient sample size to conclude that there is negligible low ion absorption at larger radii.<sup>11</sup> Future work should assess the covering fraction of low ion gas to the virial radius (and beyond) for  $L \approx L^*$  galaxies.

One cannot draw strong conclusions on the behavior of the low ions for the smaller, non-SF sample. There is a low detection rate at  $R < 75$  kpc (1/4 sightlines), but a comparable or even higher rate of detection than the SF sample at  $R > 75$  kpc. The dominant factor in a positive detection appears to be the  $N_{\text{H I}}$  value, which is uncorrelated with  $R$  for this small set of galaxies.

We now consider how the low ion absorption relates to other absorption properties of the system and characteristics of the associated galaxies. We derive the quantity  $N_{\text{Low}}$  for each system, defined as follows: (1)  $N_{\text{Low}} = N(\text{Si}^+)$ , if the  $\text{Si}^+$  measurement is a value or lower limit; (2)  $N_{\text{Low}} = N(\text{Mg}^+)$ , if the  $\text{Si}^+$  measurement is an upper limit (or there is none recorded) and a  $\text{Mg}^+$  measurement exists. We choose  $\text{Si}^+$  as the primary ion because it has multiple transitions in the far-UV bandpass with a range of oscillator strengths yielding more reliable column density estimates. The Mg II doublet, meanwhile, offers more sensitive upper limits. Because we measure  $N(\text{Si}^+) \approx N(\text{Mg}^+)$  in cases where both are measured, we apply no offset when adopting one versus the other. In all, there are roughly half of the systems in each category.

In Figure 5, we plot  $N_{\text{Low}}$  against  $N_{\text{H I}}$  for the full sample. Despite the preponderance of limits, there are several results to glean from the measurements (illustrated, in part, by the dashed and dotted lines in the figure). First, there is a complete absence of systems with  $N_{\text{H I}} \geq 10^{16} \text{ cm}^{-2}$  and  $N_{\text{Low}} < 10^{12.3} \text{ cm}^{-2}$ . In fact, only 2 of the 12 systems with these  $N_{\text{H I}}$  values have  $N_{\text{Low}} < 10^{13.3} \text{ cm}^{-2}$ . This suggests a low incidence of metal-poor gas in the CGM of  $L^*$  galaxies (e.g., Ribaud et al. 2011). Second, with only one exception, sightlines definitively

exhibiting  $N_{\text{H I}} \leq 10^{16} \text{ cm}^{-2}$  (ignoring lower limits) are all consistent with having  $N_{\text{Low}} < 10^{12.3} \text{ cm}^{-2}$ . (One notable counterexample from the literature is the sightline studied by Tripp et al. 2011, which has many components with  $N_{\text{H I}} \leq 10^{16} \text{ cm}^{-2}$  and very extensive low ion absorption.) While in principle this could result from lower metallicity at lower  $N_{\text{H I}}$ , we suspect this result follows from the ionization state of the gas possibly combined with a lower surface density of total hydrogen. Third, all systems with  $N_{\text{Low}} \geq 10^{13} \text{ cm}^{-2}$  are consistent with  $N_{\text{H I}} > 10^{16} \text{ cm}^{-2}$  and all systems with  $N_{\text{Low}} < 10^{13.3} \text{ cm}^{-2}$  have  $N_{\text{H I}} < 10^{16} \text{ cm}^{-2}$ . In at least rough terms, therefore,  $N_{\text{H I}} = 10^{16} \text{ cm}^{-2}$  demarcates a relatively rapid transition from significant to nearly negligible low ion absorption. By the same token, the presence of significant low ion absorption (e.g., a Mg II doublet) implies gas with a non-negligible opacity at the Lyman limit, at least for sightlines intercepting the CGM of an  $L^*$  galaxy.

Turning to the relation of low ion absorption with galaxy properties, the top two panels of Figure 6 plot  $N_{\text{Low}}$  against (a) SFR and (b) stellar mass, with the symbol size inversely proportional to the impact parameter. In terms of SFR, there may be a general trend of lower  $N_{\text{Low}}$  values (average or median) with decreasing SFR, but there is substantial scatter at all values. This scatter appears well correlated with  $R$  for the SF galaxies, but possibly anti-correlated with  $R$  for the non-SF galaxies. In any case, we conclude that it is unlikely that SFR is a dominant factor driving the strength of low ion absorption, which runs contrary to the inferences drawn by Ménard & Chelouche (2009).

In contrast, the  $N_{\text{Low}}$  values appear well correlated with stellar mass, indicating that there is more circumgalactic gas in more massive galaxy halos. For example, the galaxies with  $M_* > 10^{11} M_\odot$  show the highest  $N_{\text{Low}}$  values and a high incidence of positive detections (6/7) even though the sample is almost exclusively red, non-SF galaxies. Meanwhile, the non-SF galaxies with  $M_* < 10^{11} M_\odot$  are dominated by non-detections. In fact, restricting the evaluation to the non-SF galaxies, there is a significant trend with  $M_*$ . Even with the small sample size, the non-SF galaxies with  $M_* < 10^{11} M_\odot$  have a distribution of  $N_{\text{Low}}$  values that differs from the  $M_* > 10^{11} M_\odot$  at 95% confidence. This cannot be simply attributed to differences in impact parameter between the two subsamples. Despite an apparent trend of decreasing  $N_{\text{Low}}$  with decreasing  $M_*$  for the SF galaxies with  $M_* < 10^{11} M_\odot$ , the null hypothesis of no correlation is not ruled out at very high confidence (94%) by a generalized Kendall-tau test. If such a trend exists, it will require a larger sample of galaxies, possibly controlled for impact parameter.

#### 4.2. Intermediate Ions

For the purposes of this work, we define an “intermediate ion” as the first species of an element which requires an excess of 1 Ryd in energy to produce it. For example, the intermediate ions of C and Si are  $\text{C}^{++}$  and  $\text{Si}^{++}$ , which require 24.4 and 16.3 eV of energy, respectively, to ionize the previous (low ion) stage. Owing to their higher ionization potential, one predicts that these ions trace more highly ionized gas, e.g., the inner portions of an H II region.

In the far-UV, there are two particularly strong transitions from these intermediate ions, Si III  $\lambda 1206$  and C III  $\lambda 977$ . Measurements of their equivalent widths and column densities for the COS-Halos sample are presented in Figure 7. It is immediately evident that the sightlines show a high covering fraction, even exceeding the observed values for the low ions.

<sup>10</sup> Taking the lower limits on  $N(\text{Mg}^+)$  as standard detections.

<sup>11</sup> Of course, the presence of neighboring galaxies will preclude zero absorption.

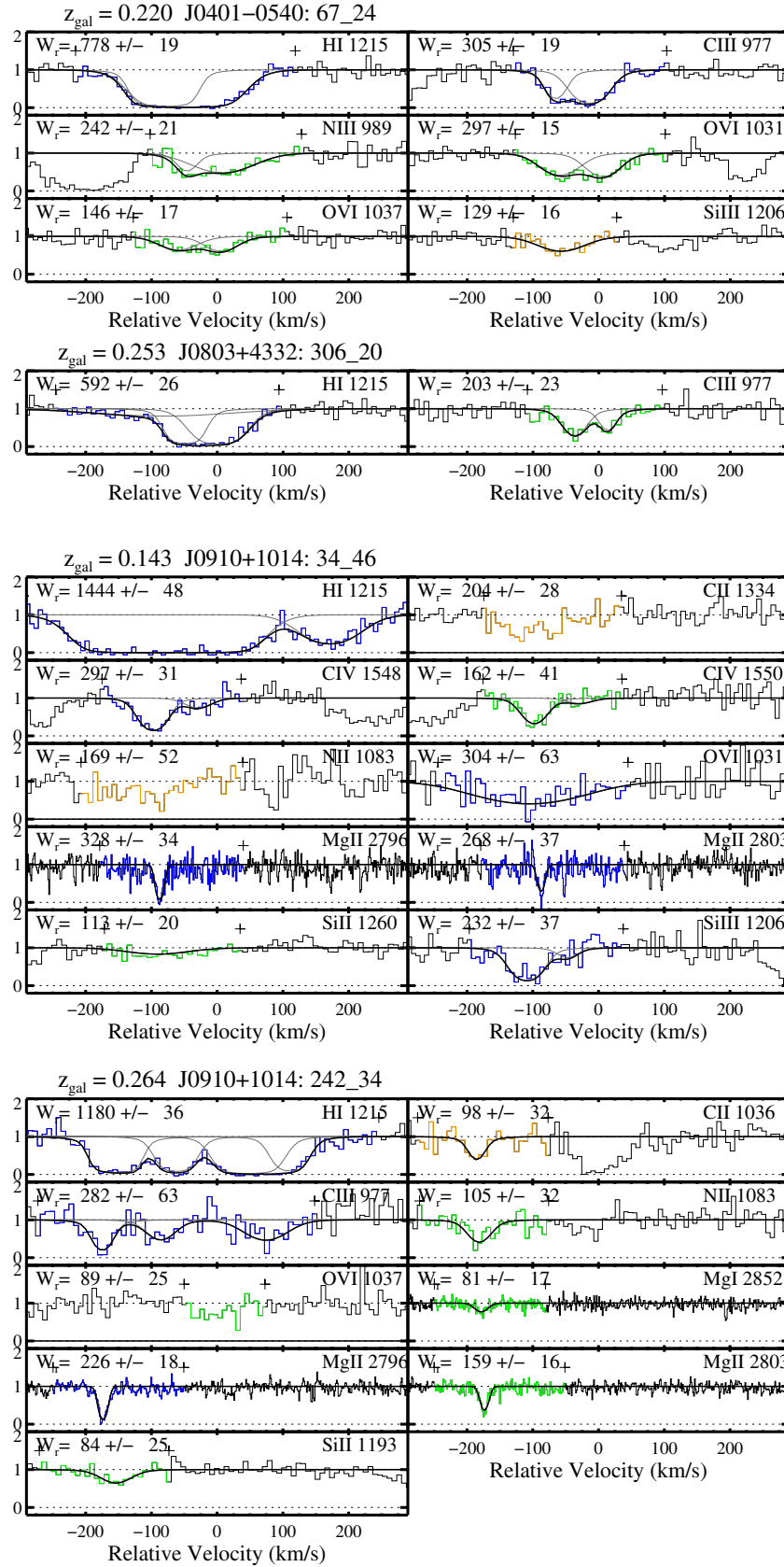


**Figure 3.** Ionic species stack plots drawn from the COS and Keck spectra, centered on the absorption lines included in the analysis. Multi-component Voigt profile fits to individual absorption lines are shown, where applicable. The X-axis ranges from  $\pm 300 \text{ km s}^{-1}$  from the associated galaxy redshift. Absorption lines are highlighted in color. Green signifies a good, uncorrupted detection; blue indicates the line is saturated; orange indicates the line is blended with some intervening absorption (often from the MW); and red shows lines that are both saturated and blended. The plus symbols mark the velocity range over which we define the absorption.

(A color version of this figure is available in the online journal.)

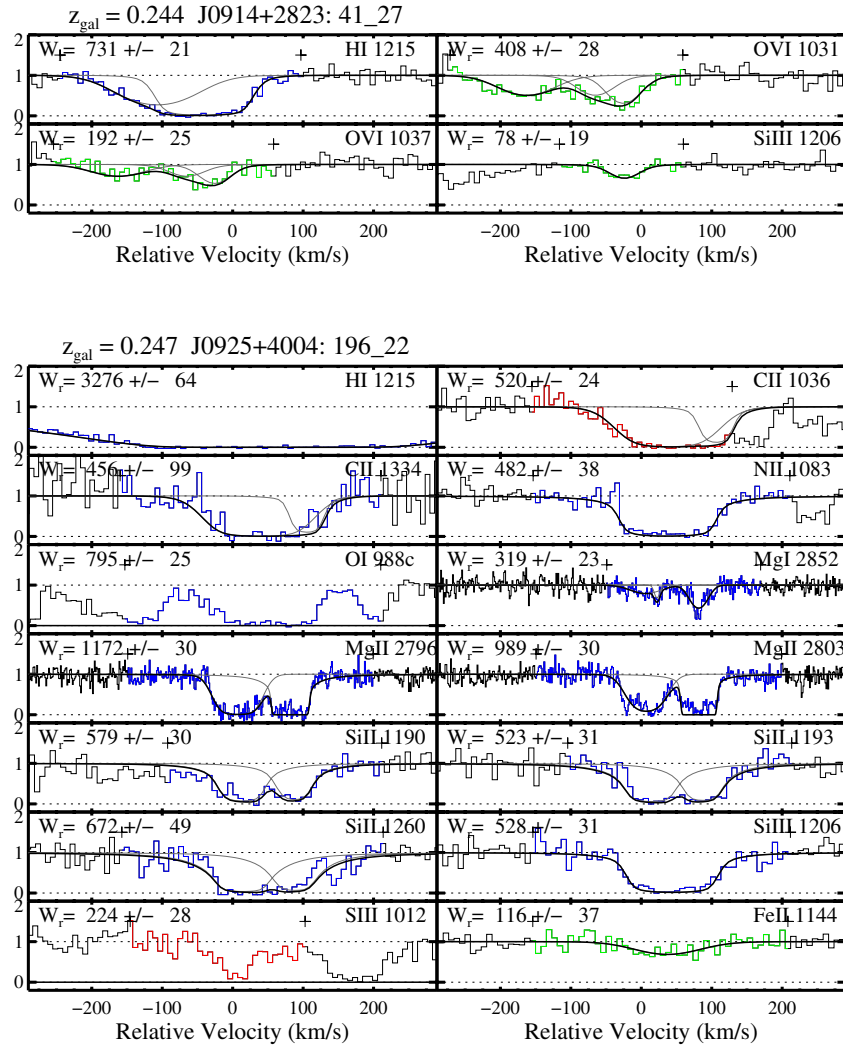


Figure 3. (Continued)

For C III 977, the SF galaxies exhibit a nearly 100%  $C_f$  (Tables 5 and 6) with the only non-detection in 14 cases having  $R \approx 160$  kpc. Within  $R = 50$  kpc, the results are especially striking. The SF galaxies uniformly exhibit equivalent widths  $W_{977} > 400$  mÅ corresponding to lower limits on  $N(C^{++})$  of  $10^{14.2} \text{ cm}^{-2}$  and higher. Some of the values may even exceed the observed H I column densities.

The results for Si<sup>++</sup> are similar, albeit with a greater dynamic range of equivalent widths and column densities, and somewhat lower  $C_f$  values. Si<sup>++</sup> ( $f_{\lambda,1206} = 1.660$ ) has a larger oscillator strength than Si<sup>+</sup> ( $f_{\lambda,1260} = 1.007$ ), which may play a role in this difference. Nonetheless, the greater dynamic range reveals a key result: the absorption strength of intermediate ions is highly correlated with impact parameter. Restricting to the positive detections of the SF galaxies and treating all of these as values,<sup>12</sup> we measure a Spearman's rank correlation of  $-0.65$  and  $-0.69$  for  $W_{1206}$  and  $N(\text{Si}^{++})$  versus  $R$  implying an anti-correlation at 99.95% and 99.99% confidence. Motivated by the strong anti-correlation, we modeled the radial variation in  $W_{1206}$  and

$N(\text{Si}^{++})$  with single power-law expressions:

$$W_{1206} = W_{(10 \text{ kpc})} \left( \frac{R}{10 \text{ kpc}} \right)^{\alpha_W}, \quad (1)$$

$$N(\text{Si}^{++}) = N_{(10 \text{ kpc})} \left( \frac{R}{10 \text{ kpc}} \right)^{\alpha_N}. \quad (2)$$

In each case, we have restricted the analysis to the positive detections and have taken lower limits at their measured value. Minimizing  $\chi^2$  with equal weighting for each measurement, we derive  $\log W_{(10 \text{ kpc})} = 0.13 \pm 0.44$ ,  $\alpha_W = -0.84 \pm 0.24$  and  $\log N_{(10 \text{ kpc})} = 14.1 \pm 0.2$ ,  $\alpha_N = -1.11 \pm 0.29$ . This simple model is overplotted on the data in Figure 8. The preponderance of lower limits to  $N(\text{Si}^{++})$  at  $R < 50$  kpc implies a even higher  $\log N_{(10 \text{ kpc})}$  and steeper  $\alpha_N$  values than reported by this simple analysis. We discuss the implications and possible origins of this central result in Section 5.

Regarding the non-SF galaxies, the incidence of positive detections for the intermediate ions is lower than that observed for the SF galaxies, with  $C_f \approx 50\%$  for Si<sup>++</sup> and C<sup>++</sup>. On the other hand, the equivalent widths and column densities of the positive detections are comparable or even higher than those for the SF galaxies. This gives a bimodal distribution in the

<sup>12</sup> A proper treatment of the limits, lower and upper, would only strengthen the statistical significance.

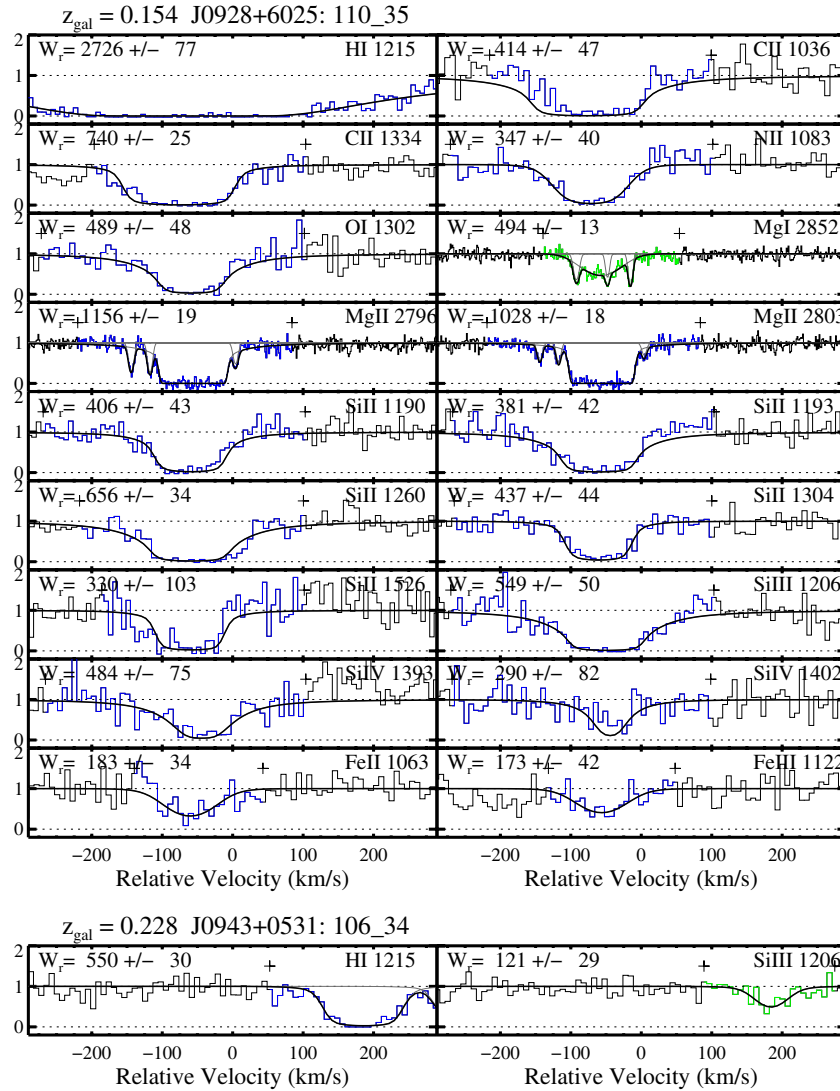


Figure 3. (Continued)

non-SF galaxy subset which is not evident in the SF galaxy sample (Figure 9). The implication is that the gas is either less smoothly distributed within individual halos of non-SF galaxies and/or that there is a bimodal separation in the CGM amongst the galaxies themselves. A similar result holds for  $C^{++}$  as well. A less likely option to explain this result would be that all of the non-SF galaxies for which we have detected low and intermediate ion absorption have a fainter, SF galaxy in their vicinity that is associated with the gas. We have not completed a redshift survey of all faint sources in the COS-Halos quasar fields, and the SDSS images are not sensitive to galaxies fainter than  $0.1L^*$  at  $z \sim 0.2$ , so it is impossible to comment in detail about this option. However, we do note that a visual inspection of the SDSS images of the non-SF galaxy QSO fields yields very few additional blue  $L > 0.1L^*$  candidates within  $2'$ . Even if there are other SF galaxies in their vicinity, the CGM gas is nonetheless physically associated with the elliptical and very likely bound to its dark matter halo. Establishing the origin of the CGM is beyond the scope of this empirically focused paper.

To explore further the characteristics of the intermediate ions, we plot in the lower two panels of Figure 6  $N(\text{Si}^{++})$  against the (c) SFR and (d) stellar mass of the associated galaxies.

Similar to the low ion absorption, there is no obvious correlation with intermediate ion column density and SFR. Regarding  $M_*$ , however, one identifies notable trends. Restricting first to the SF population, the  $N(\text{Si}^{++})$  values appear correlated with  $M_*$ ; the null hypothesis is ruled out at 99% confidence by a generalized Kendall-tau correlation test. Similarly, the median column density for  $M_* > 10^{10.5} M_\odot$  is  $\tilde{N}(\text{Si}^{++}) = 10^{13.4} \text{ cm}^{-2}$  and  $\tilde{N}(\text{Si}^{++}) = 10^{12.9} \text{ cm}^{-2}$  for  $M_* < 10^{10.5} M_\odot$ . Within the non-SF population, there is a preponderance of low  $N(\text{Si}^{++})$  values for  $M_* < 10^{11} M_\odot$  (6/8). Indeed, this stands in stark contrast to the SF population. The notion of a correlation, however, is tempered by several positive detections at these masses. Another notable result revealed by Figure 6 is that the quiescent galaxies are well separated from the SF galaxies within the  $M_*$  panels, both low and intermediate ions.

In concluding this section, we compare the column densities and component structure of the low and intermediate ions. We supplement this analysis by comparing these profile fits with those of  $\text{O}^{+5}$  (Tumlinson et al. 2011). Figure 10 plots the  $N(\text{Si}^+)/N(\text{Si}^{++})$  and  $N(\text{C}^+)/N(\text{C}^{++})$  ratios against two quantities that may be expected to correlate with the ionization state of the gas: H I column density and the SFR scaled inversely by the impact



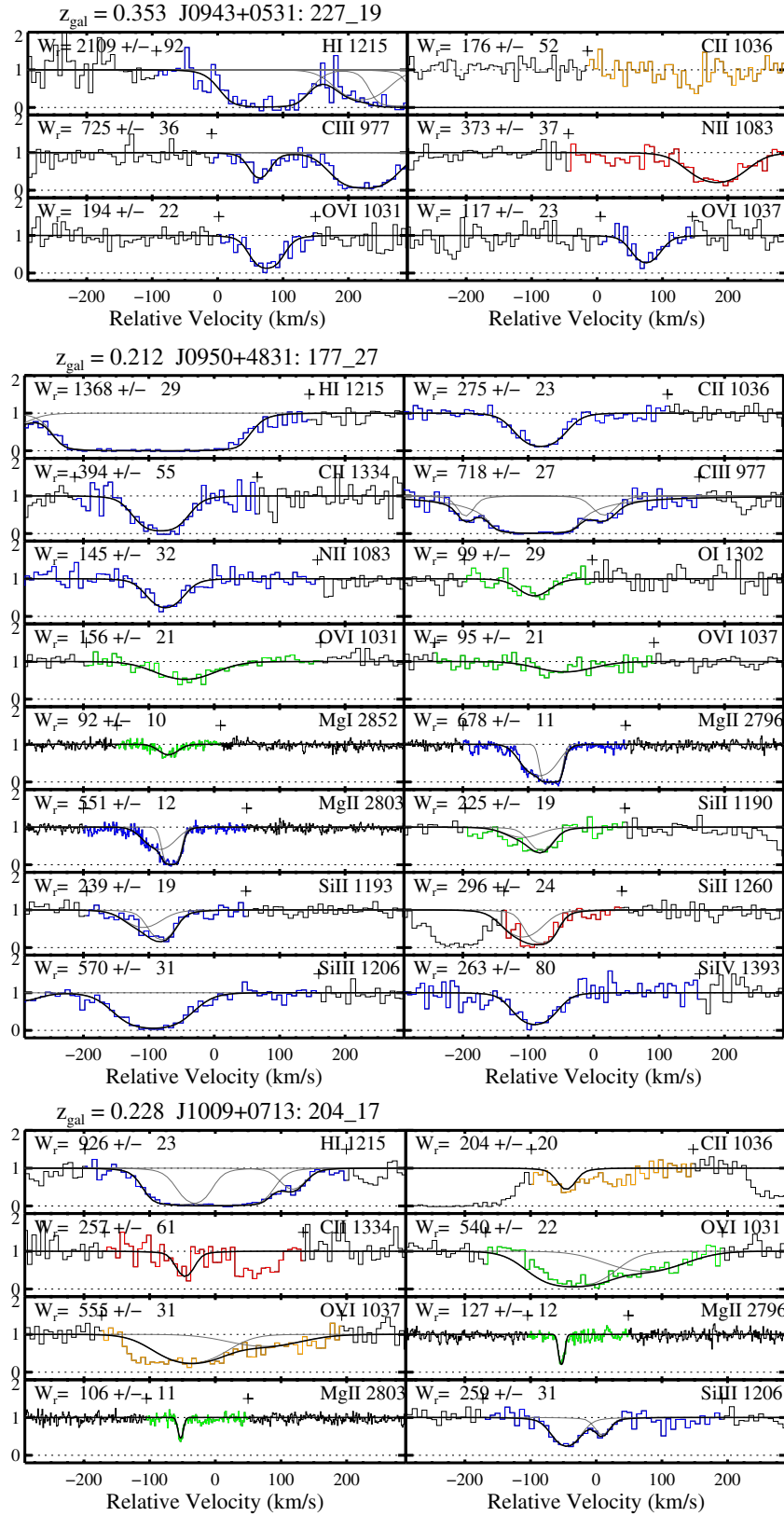


Figure 3. (Continued)

parameter squared. For the former, one expects stronger low ion absorption as  $N_{\text{H I}}$  increases and the gas becomes optically thick to ionizing radiation. The quantity  $\text{SFR}/R^2$ , meanwhile, represents an estimate of the ionizing flux from massive stars.

This assertion is subject, of course, to uncertainties in the escape fractions of galaxies, to error in using  $R$  as the distance from source to gas, and to the relative flux of the galaxy to the extragalactic UV background.

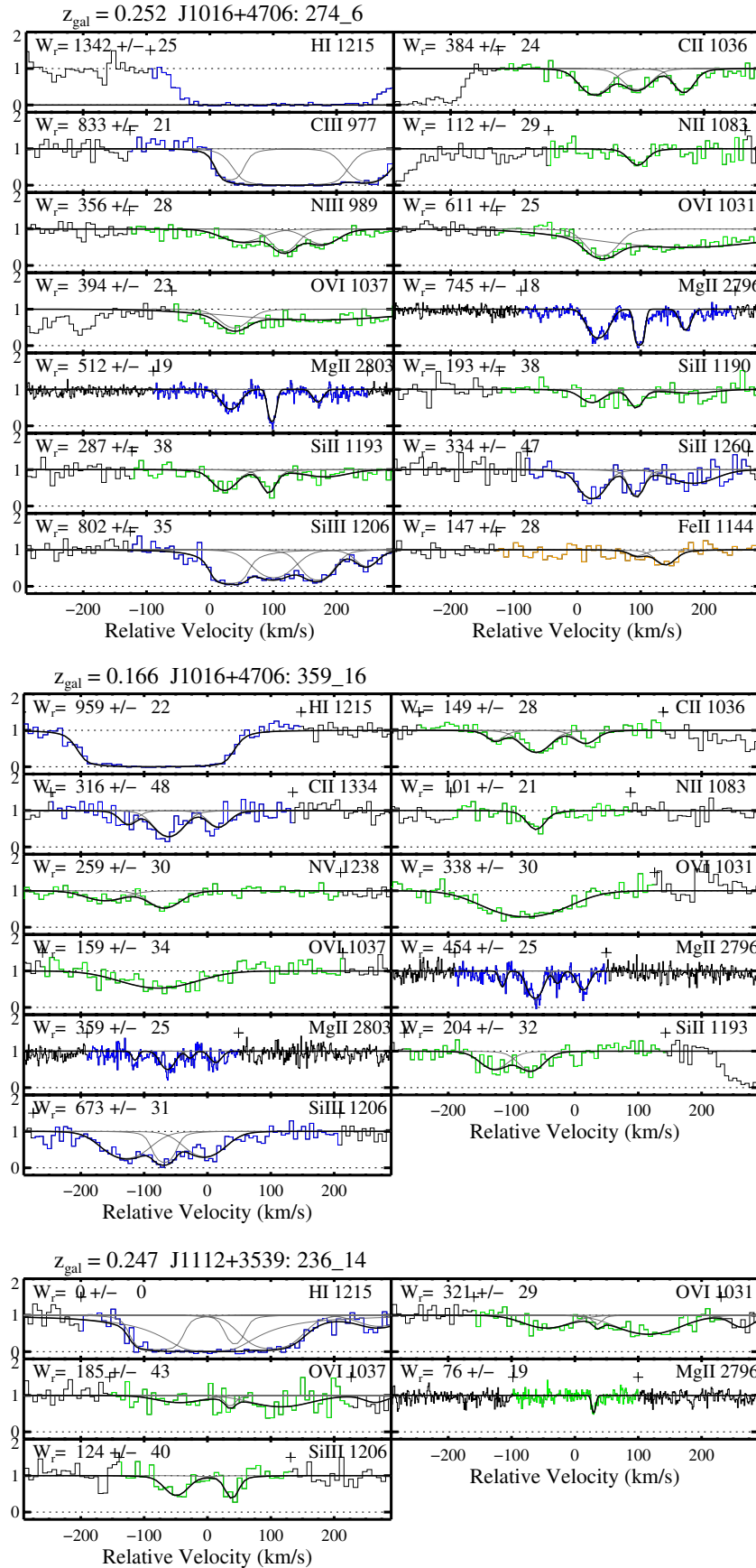


Figure 3. (Continued)

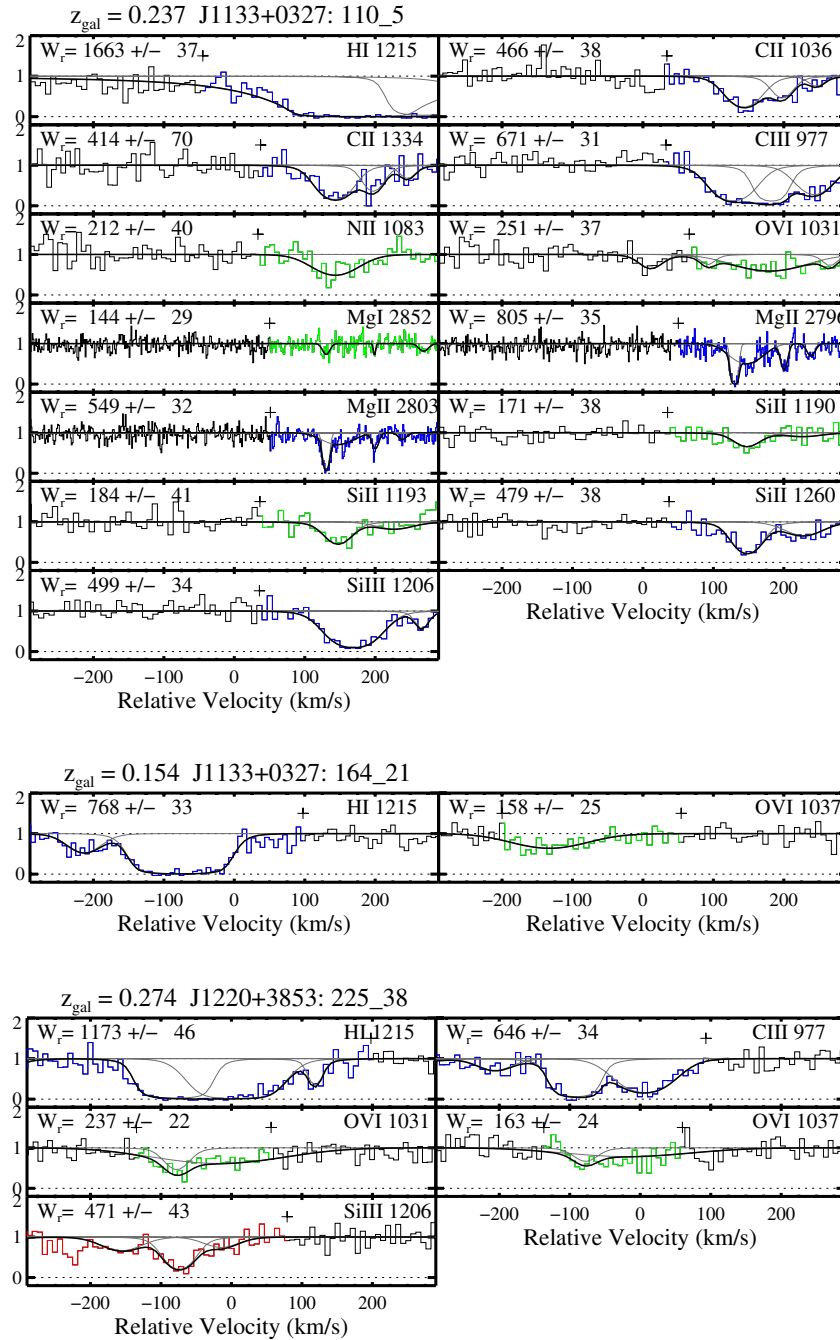


Figure 3. (Continued)

The main point to emphasize from Figure 10 is that the  $N(\text{Si}^+)/N(\text{Si}^{++})$  ratios are uniformly low; nearly every system<sup>13</sup> is consistent with  $N(\text{Si}^+)/N(\text{Si}^{++}) < 1$ . If the gas arises in a single phase, this requires that the majority of CGM gas is significantly ionized. One draws the same conclusion from the observed  $N(\text{C}^+)/N(\text{C}^{++})$  ratios. Inspection of Figure 10 also reveals there are no obvious trends with  $\text{SFR}/R^2$  or  $N_{\text{H I}}$ . Perhaps the only noteworthy observation in this regard is that the two systems with  $N(\text{Si}^+)/N(\text{Si}^{++})$  exceeding unity have amongst the lowest  $\text{SFR}/R^2$  values in the SF population.

If the low and intermediate ions arise from a single phase, then one would expect the kinematic component structure of

their absorption profiles to be similar. We may test this prediction through an analysis of the profile fits generated from the absorption lines (Table 4). As we impose no restrictions on the component structure between different ionization states of the same element, any qualitative and quantitative similarities between the fits arise naturally. Indeed, a visual inspection of the fitted absorption features indicates strong similarities between low and intermediate ionization states of Si, C, and N (Figures 3 and 11). Errors in the COS wavelength solution should only weaken such correlations. Generally, the intermediate ion absorption tends to be stronger than the low ion absorption in the CGM of  $L^*$  galaxies, but there is no evidence that the low and intermediate ionic absorption arise from different gas phases based on their component structure alone.

<sup>13</sup> We caution that 5 systems have lower limits to both  $N(\text{Si}^+)$  and  $N(\text{Si}^{++})$  and 13 systems have non-detections for both ions.

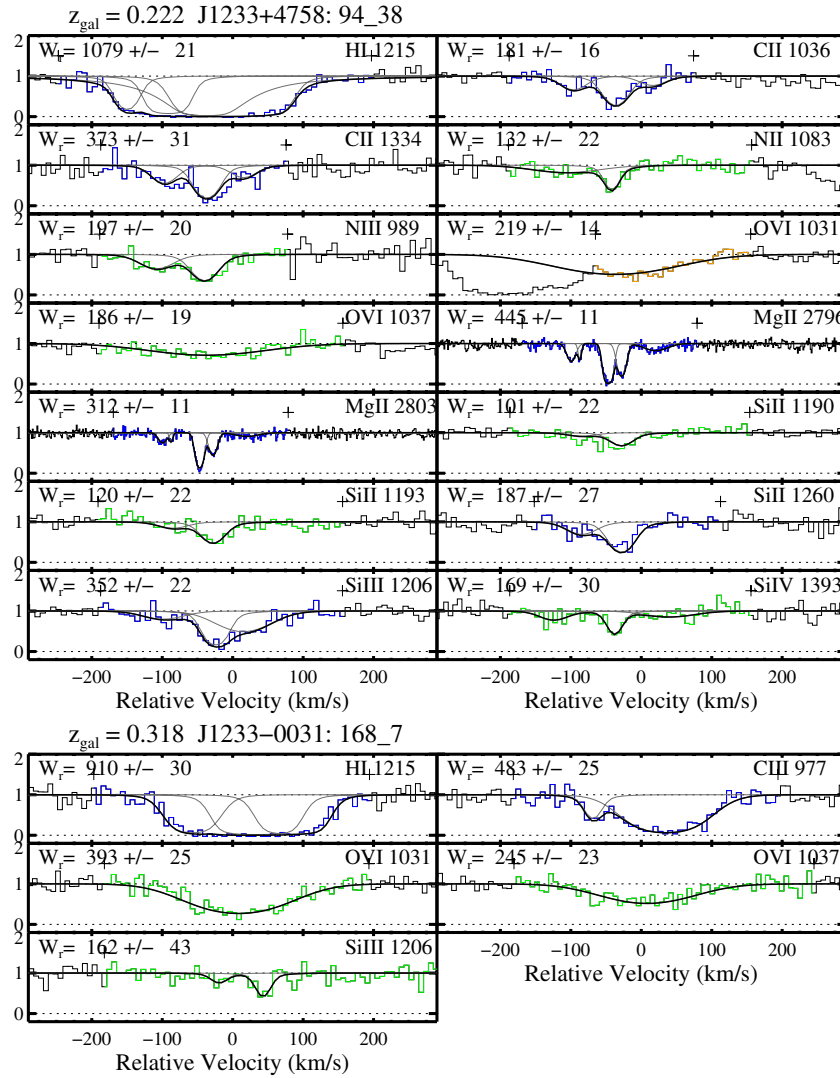


Figure 3. (Continued)

We have also shown in Figure 11 the profile fits to the  $O^{+5}$  absorption line, which were derived from our COS data set and analyzed previously by Tumlinson et al. (2011). Unlike the clear correspondence between the black (low ion) and red (intermediate ion) lines, a qualitative assessment of the overall agreement and component structure of the blue (high ion:  $O^{+5}$ ) lines is complex. In nearly all cases, the individual fitted components of the  $O^{+5}$  absorption lines are broader than those of the lower ionization states, but there is generally good correspondence between the shape and number of components. There are impressive alignments (e.g., J1419+4207 132\_30; J1009+0713 204\_17), but just as many, if not more, complete misalignments (e.g., J1330+2813 289\_13; J1435+3604 68\_12). This comparison suggests that the relationship between low and high ionization states of gas along the same sightlines is not straightforward, and commenting further here is beyond the scope of this paper. Future work will perform a quantitative comparison of these profiles and examine the implications for the origins and overlap of this broad range of circumgalactic gas ionization states.

#### 4.3. Covering Fraction ( $C_f$ )

A valuable measure of assessing the distribution of absorption by the CGM is through estimations of the covering fraction  $C_f$ .

Strictly speaking, the  $C_f$  value describes the fraction of random sightlines that pass within a given impact parameter to a galaxy (or population of galaxies) that exhibit a specified absorption strength for a given transition or ion. For example, one can measure the fraction of sightlines exhibiting  $W_{r,2796} > 0.3 \text{ \AA}$  when passing within<sup>14</sup> 50 kpc of a SF  $L^*$  galaxy at  $z = 0$ . The covering fraction assesses how gas in the CGM is distributed (as projected on the sky), gives a rough assessment of the strength of absorption, and reduces complex distributions to a single number. Furthermore, it presents a simplified target for theoretical models to consider.

Despite its apparent simplicity, estimating the  $C_f$  values for the equivalent width of a specific transition or the column density of a given ion is non-trivial. This is due to several factors. First, we have a limited sample of galaxies under study and cannot claim to have a complete sample, nor (necessarily) even a fully representative sample of any given population. Second, we have limited sampling of the CGM on scales of  $R < 30 \text{ kpc}$ . Third, the projected area scales with radius whereas we designed the

<sup>14</sup> In principle, one must also define  $C_f$  over a velocity interval relative to the galaxy. This is important for H I absorption where one may be confused by the IGM. Heavy elements are sufficiently rare, however, that the results presented here are insensitive to this issue provided that one chooses a sufficiently large window ( $> 300 \text{ km s}^{-1}$ ).



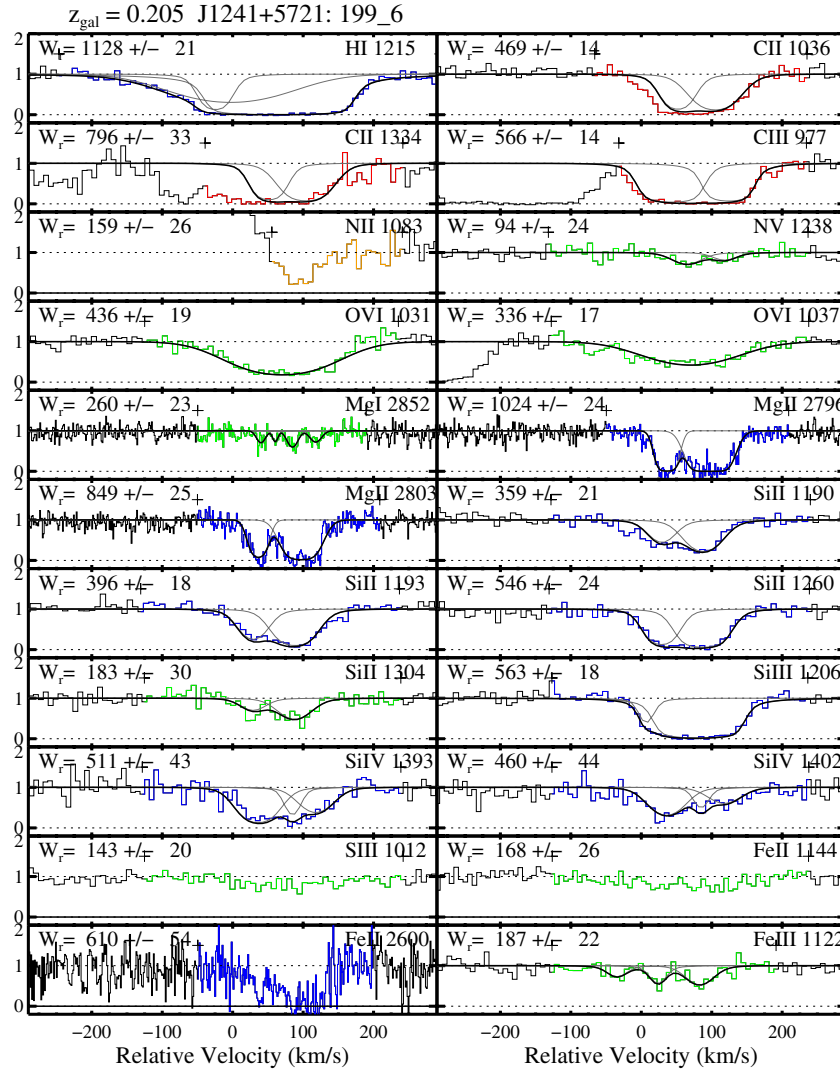


Figure 3. (Continued)

COS-Halos project to uniformly sample impact parameter from  $R \approx 30$  to 160 kpc. A strict comparison of models to our data set must account for these issues. Lastly, both the equivalent width and column density measurements include a mix of measurements and upper/lower limits. Given these limitations, we proceed conservatively.

For the covering factors relating to the equivalent width measured for a specific transition (e.g.,  $W_{r,2796}$ ,  $W_{r,1334}$ ), we chose thresholds that exceeded nearly all of the observed upper limits. These values are listed in Column 4 of Table 5. In cases where an upper limit exceeds this threshold, we included that measurement as if it exceeds the threshold, thereby increasing  $C_f$ . The error reported in  $C_f$ , which follows a standard binomial Wilson score, accounts for this uncertainty by calculating the 68% confidence interval assuming that upper limits above the threshold do not satisfy it.

The evaluation of  $C_f$  for column density measurements are more challenging because they often include a mix of upper and lower limits (Table 6). Again, we aimed for a column density threshold that exceeded the upper limits while not exceeding the lower limit values. Similar to the  $C_f$  for  $W_r$  values, we treated upper limits above the threshold as detections. We also considered lower limits below the line as satisfying the threshold. In

this respect the resultant  $C_f$  values may be considered maximal, aside from the uncertainty of Poisson statistics.

In Figure 12, we present a comparison of the  $C_f$  values for transitions spanning a wide range of ionization state. The results for H I and O<sup>+</sup> are drawn from the J. Tumlinson et al. (in preparation) and Tumlinson et al. (2011) papers, respectively. It is evident that the H I gas exhibits the highest covering fraction, not only for the SF galaxies;  $L^*$  galaxies of all spectral type exhibit a CGM of cool, hydrogen gas (Thom et al. 2012). Examining the metal-line transitions, which are arranged from lowest to highest ionization potential, one observes a significant covering ( $C_f > 0.5$ ) for all ions and populations except O<sup>+</sup> for the non-SF galaxies (Tumlinson et al. 2011). This demonstrates significant metal enrichment throughout the CGM of  $L^*$  galaxies. It further suggests a multi-phase medium because it is nearly physically impossible to find strong low ion and O<sup>+</sup> absorption in the same gas. One also observes a trend of increasing  $C_f$  with increasing ionization state. For the SF galaxies, there is a monotonic increase in  $C_f$  from 60% in the low ion species to nearly 90% for the highly ionized O<sup>+</sup> gas. This implies that the gas is significantly ionized. The non-SF galaxies also show increasing  $C_f$  until O<sup>+</sup> where one finds much less gas (Tumlinson et al. 2011). The CGM of quiescent  $L^*$

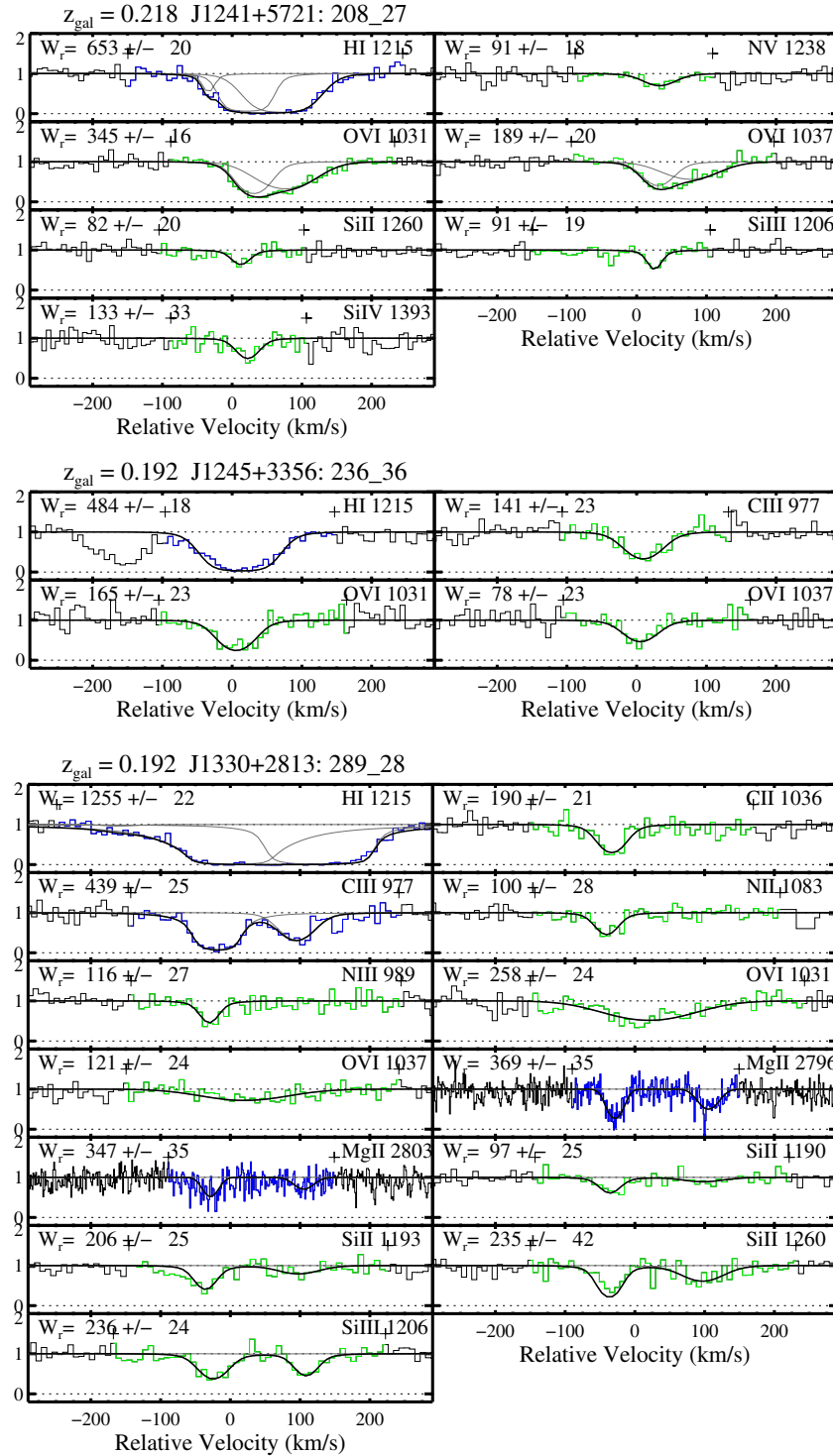


Figure 3. (Continued)

galaxies is also enriched, but that there is a qualitative difference between the two populations at the highest ionization states.

We explore variations in  $C_f$  with impact parameter in the lower panel of Figure 12. Within the SF population (blue), there is a clear difference between the two radial cuts for metals such that the metal covering fraction is lower for higher impact parameters. While a declining metallicity gradient could be responsible, this trend is more likely the result of the decreasing total gas surface density with radius (J. K. Werk et al., in preparation). Oddly, the opposite trend is noted for the quiescent

galaxies (red). We are concerned, however, that this may be masked by the small number statistics of this sub-population.

#### 4.4. Comparison to Previous Work

As a check on our analysis, we may wish to compare our results against similar measurements from the literature. Such comparisons may reveal systematics in our line measurements or anomalies in the sample definition. Unfortunately, very few analyses have been performed on the low and intermediate ionization states of metal-line absorption in the CGM of

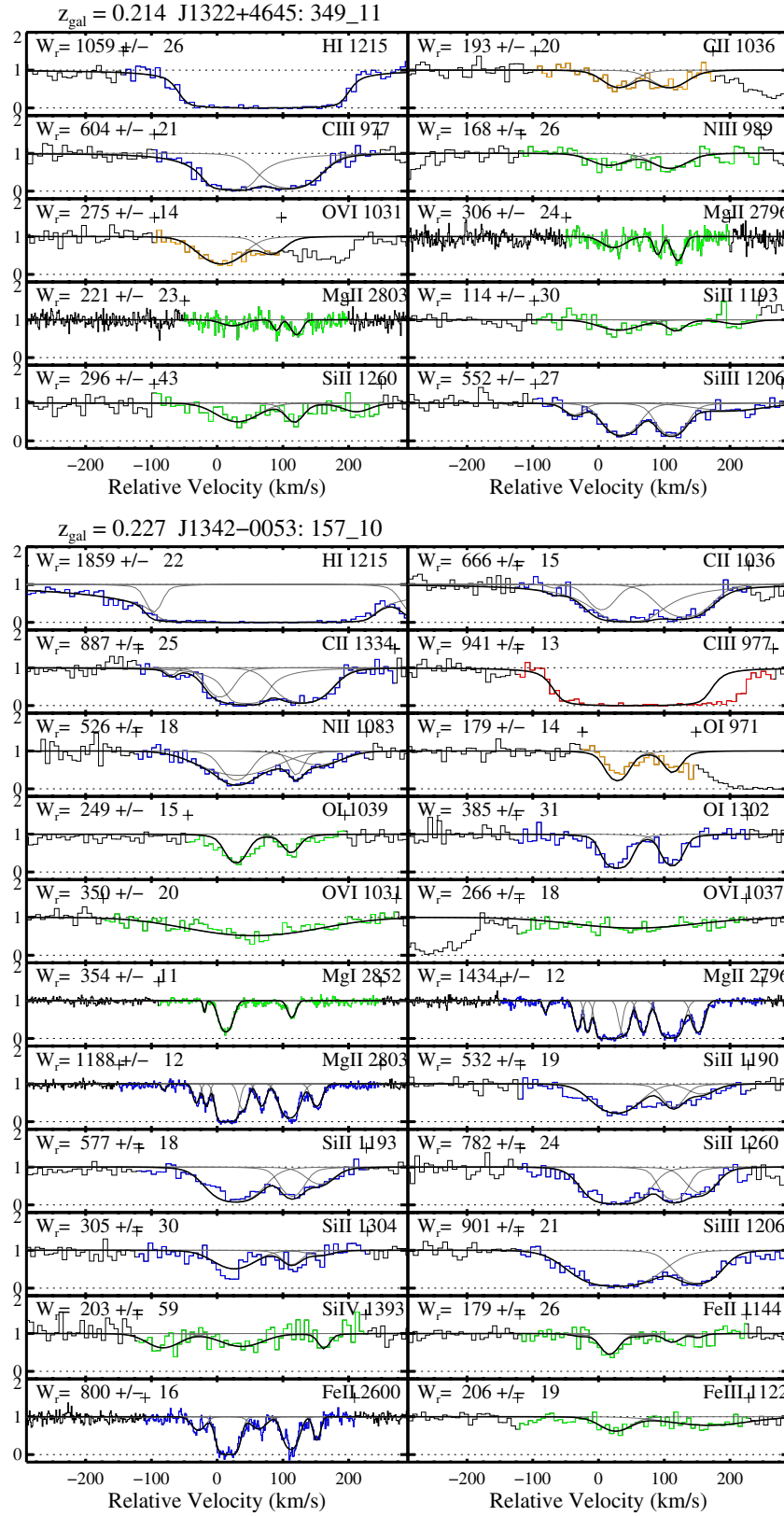


Figure 3. (Continued)

$L^*$  galaxies. The obvious exception is  $\text{Mg}^+$ , which has been extensively surveyed over the past several years (e.g., Barton & Cooke 2009; Chen et al. 2010), and to a lesser extent  $\text{C}^{+3}$  (not covered by this work), which is found to extend out to 150 kpc (Chen et al. 2001).

In Figure 13, we present a comparison of our  $W_{r,2796}$  measurements against impact parameter with those reported by Chen et al. (2010). We also plot their favored model for the variation of  $W_{r,2796}$  with impact parameter, adopting  $L = L^*$  in the calculation. Qualitatively, we find that the two data sets are in good

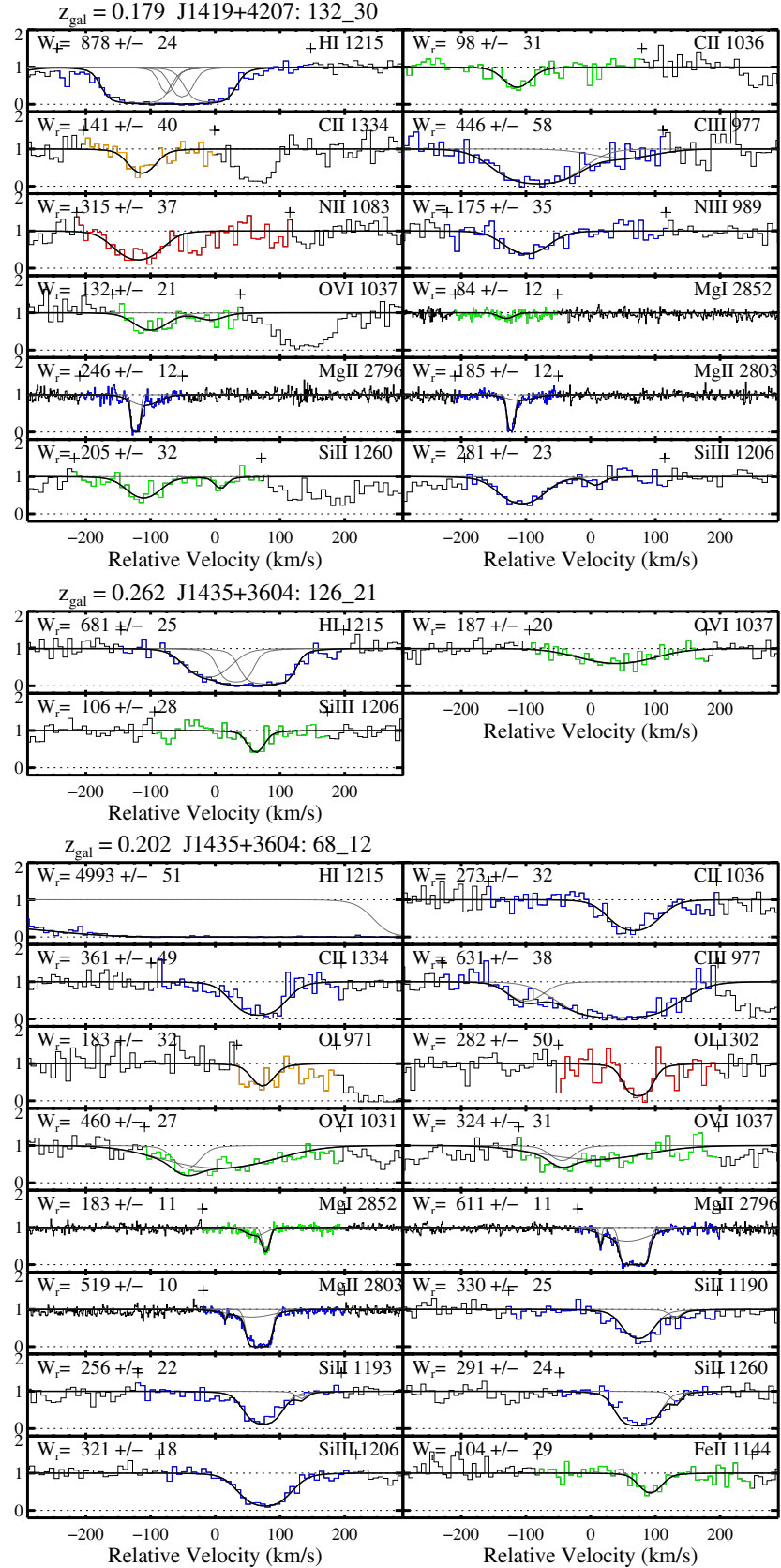


Figure 3. (Continued)

agreement. The positive detections occupy similar regions of the  $W_{r,2796}$ ,  $R$  parameter space and the upper limits occur primarily at  $R > 50$  kpc. Both data sets show a very large dispersion with respect to the  $W_{r,2796}(R)$  model; in fact, the line appears to best

describe the division between detections and non-detections at  $R > 70$  kpc. We conclude that our sample, which extends to many ions beyond  $\text{Mg}^+$ , has no especially anomalous characteristics.



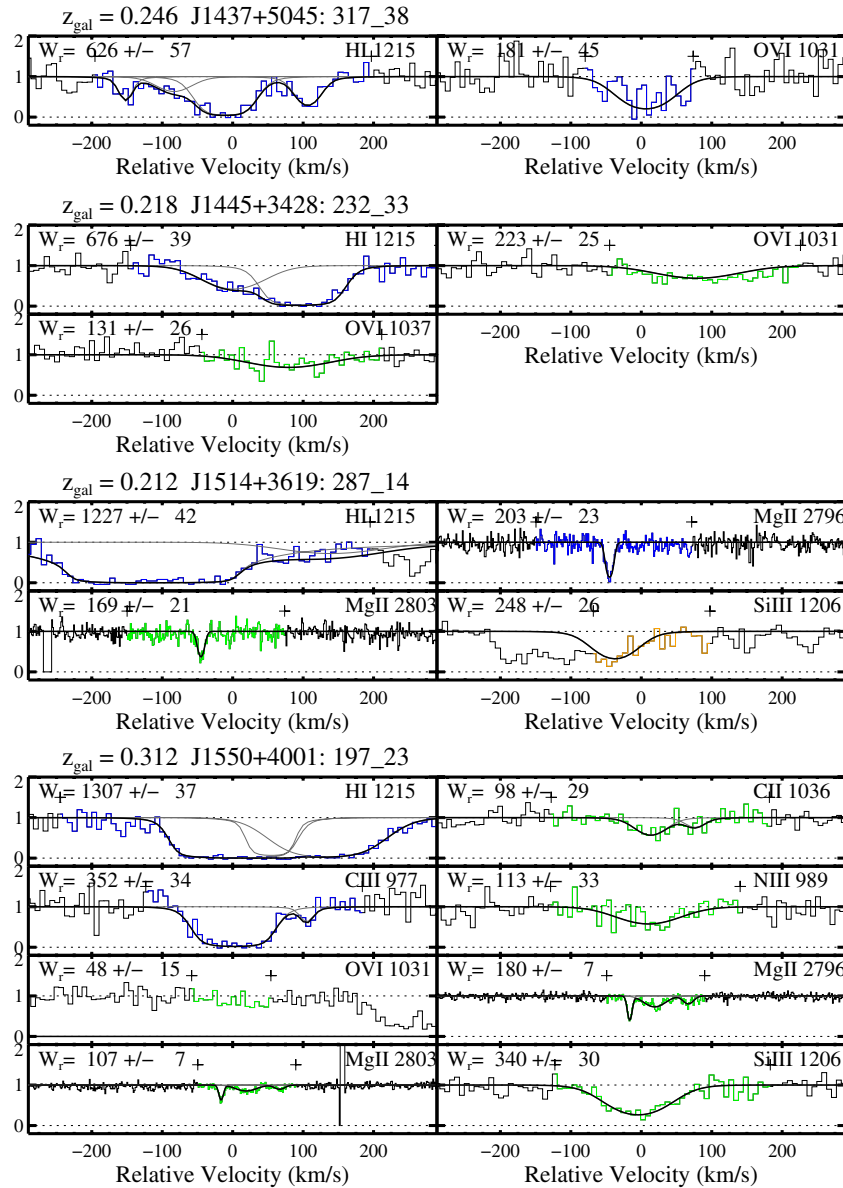


Figure 3. (Continued)

## 5. DOMINANT CHARACTERISTICS OF THE COOL CGM

In the previous section, we presented results derived primarily from measurements of the equivalent widths and column densities of low and intermediate ionization states of metals arising in the CGM of low- $z$ ,  $L \approx L^*$  galaxies. These data provide an empirical assessment of several fundamental properties of the CGM. Table 7 summarizes the absorption-line strength statistics for our sample (and various subsamples) of galaxies, giving median and average values as a function of impact parameter. Before discussing these results, we summarize key results from our previous and parallel analyses on this COS-Halos sample of galaxies to provide context.

First, nearly all of these galaxies exhibit strong ( $W_{\text{Ly}\alpha} > 0.5 \text{ \AA}$ ) Ly $\alpha$  absorption with H I column densities  $N_{\text{H I}}$  exceeding  $10^{14} \text{ cm}^{-2}$  and often  $10^{16} \text{ cm}^{-2}$  (Figure 12; Thom et al. 2012; J. Tumlinson et al., in preparation). Only 5 of the 44 sightlines analyzed in this paper have  $N_{\text{H I}} < 10^{14} \text{ cm}^{-2}$ . Second, line-profile analysis of the Ly $\alpha$  absorption yields Doppler parameters that require the H I gas to be predominantly cool, i.e.,  $T < 10^5 \text{ K}$ .

These data establish the presence of a cool CGM surrounding  $L \approx L^*$  galaxies to at least 160 kpc, consistent with previous works on H I Ly $\alpha$  (e.g., Lanzetta et al. 1995; Wakker & Savage 2009; Prochaska et al. 2011a). Third, the SF population exhibits a very high incidence ( $\geq 90\%$  to  $R = 160 \text{ kpc}$ ) of strong O $^{+5}$  absorption (Figure 12; Tumlinson et al. 2011). The measured column densities require a large mass of highly ionized gas in the CGM of these galaxies ( $M_{\text{CGM}}^{\text{high}} > 10^9 M_{\odot}$ ). In contrast, the quiescent systems show a significantly lower frequency of detected O $^{+5}$  revealing a dichotomy in the CGM that traces galaxy properties.

In this paper, we have analyzed far-UV spectra from *HST*/COS and near-UV spectra from Keck/HIRES to examine over 30 metal-line transitions of low and intermediate ionization states with ionization potentials ranging from  $\approx 5$  to 100 eV. Of the 44 galaxies analyzed (Table 1), we report positive detections for at least one metal-line transition from the CGM in 33 systems. Consistent with the O $^{+5}$  results, this demonstrates a metal-enriched CGM for  $L^*$  galaxies to at least  $R = 160 \text{ kpc}$ . In contrast to the O $^{+5}$  results, our detections frequently include the

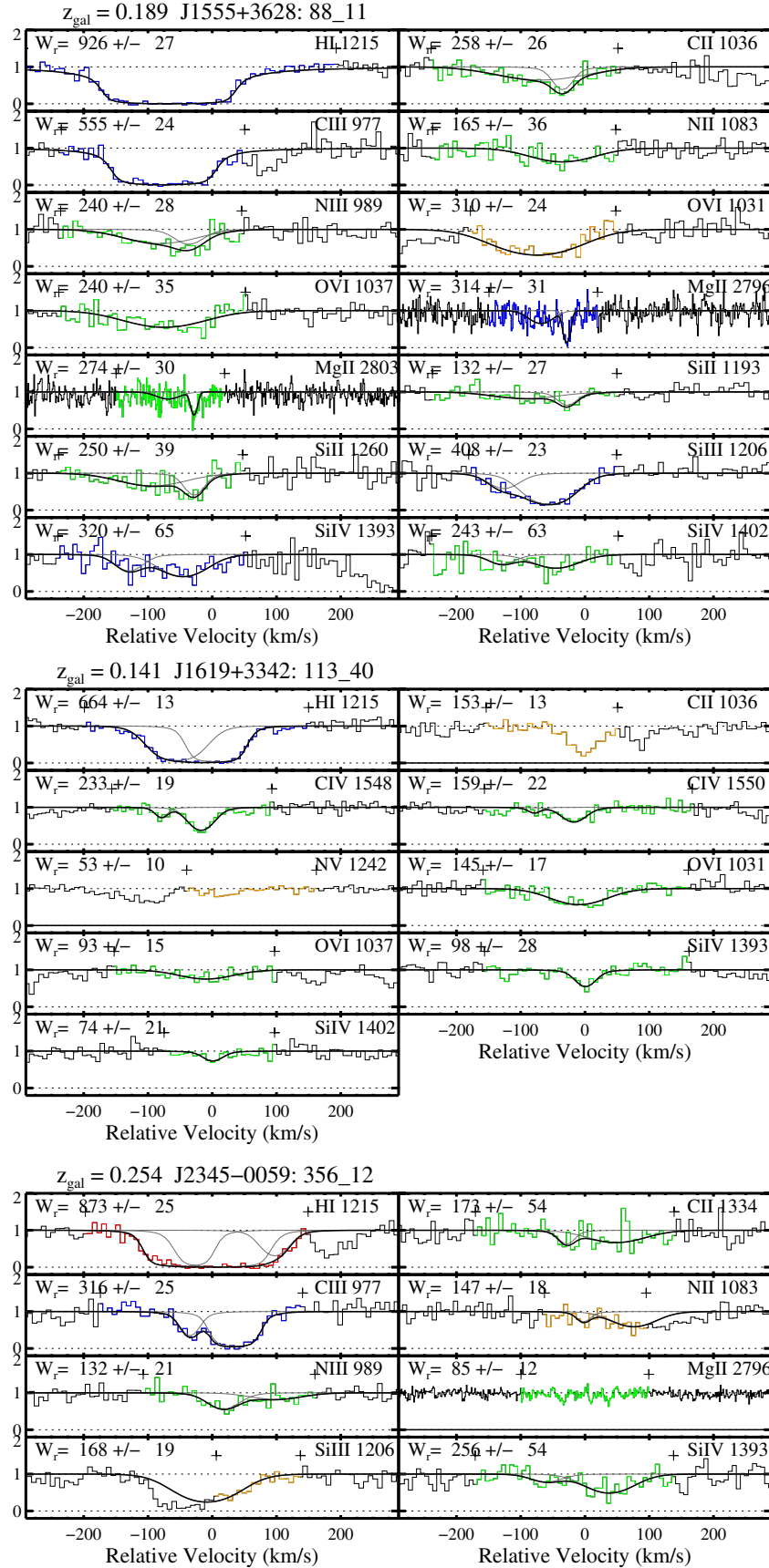
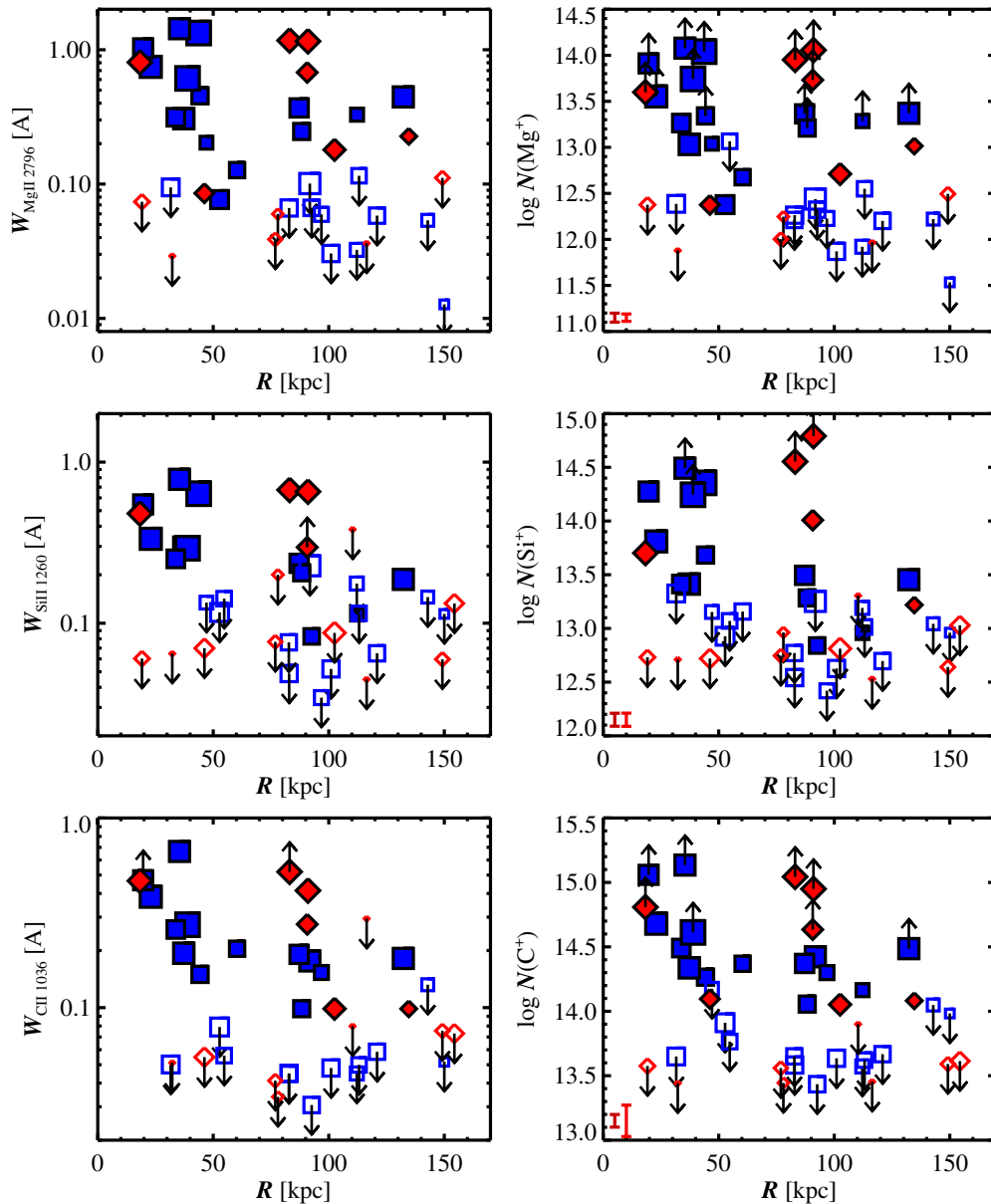


Figure 3. (Continued)



**Figure 4.** Equivalent width (left panels) and column density measurements (right panels) vs. impact parameter  $R$  of the COS-Halos sample for the set of the three most commonly detected low ions: Mg II (upper panels), Si II (middle panels), and C II (lower panels). In each panel, the symbol and color distinguish between SF (blue squares) and non-SF galaxies (red diamonds). The symbol size is linearly proportional to the  $\log N_{\text{H I}}$  value over the range  $10^{13}$ – $10^{17} \text{ cm}^{-2}$ . Open symbols with errors denote  $2\sigma$  statistical upper limits. The error bars in the lower left corner of the column density plots are representative of the measurements. Note the significant covering fraction to low ion absorption at all  $R$  values, coupled with declining  $W$  and  $N$  values with increasing  $R$ . It is also evident that the positive detections are dominated by systems with larger  $N_{\text{H I}}$  values.

(A color version of this figure is available in the online journal.)

quiescent galaxy population: 9/16 systems have positive metal-line detections, including both low and intermediate ions. By comparison, the SF population exhibits a metal-line detection rate of 23/27. Our results indicate that the absence of strong  $\text{O}^{+5}$  in quiescent galaxies is not the simple consequence of a very low metal enrichment for their halos. One must invoke other mechanisms to explain this dichotomy, presumably related to the physical conditions of the more diffuse or hotter gas.

Another fundamental property of the CGM probed by our observations is that it must be cool, i.e.,  $T < 10^5 \text{ K}$ . The positive detection of low ion transitions in 22 galaxies demands this result. Collisional ionization of gas at  $T > 10^{4.6} \text{ K}$  would yield negligible quantities of ions like  $\text{Mg}^+$ ,  $\text{C}^+$ , and  $\text{Si}^+$ , even if at solar abundance and with a large total gas column (e.g., Gnat &

Sternberg 2007). The galaxies that only exhibit intermediate ions ( $\text{C}^{++}$ ,  $\text{Si}^{++}$ ) are constrained to  $T < 2 \times 10^5 \text{ K}$  to avoid extremely large gas surface densities. Such temperatures are consistent with the measured line-widths from profile-fitting (Table 4), provided the gas has a modest ( $\approx 5$ – $10 \text{ km s}^{-1}$ ) turbulence. Furthermore, these metals trace the majority of observed H I gas, as evidenced by the line-profiles (Figure 3) and the observed trend between  $N_{\text{H I}}$  and metal column density (Figure 5). We conclude that the lower ionization states measured in this paper are physically arising in the same regions as the majority of observed H I gas. Together, these metals and H I gas form the “cool” CGM of  $L^*$  galaxies. Future work will combine the two data sets and use ionization modeling to estimate the gas metallicity in this component (J. K. Werk et al., in preparation).

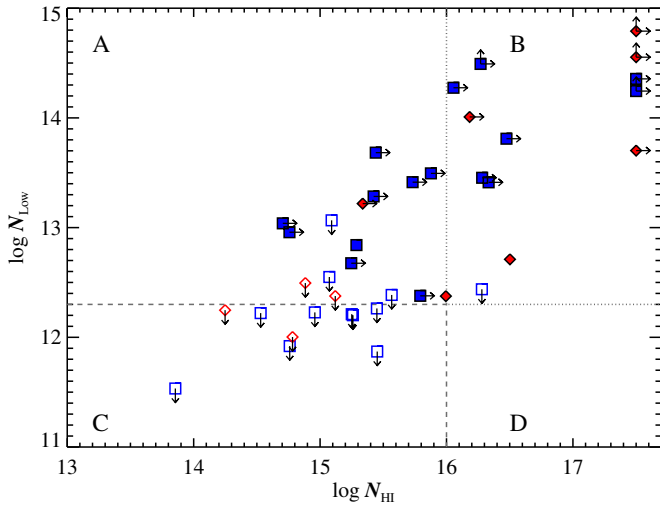


**Figure 5.**  $N_{\text{Low}}$  value, generally  $N(\text{Si}^{++})$  for values and lower limits and  $N(\text{Mg}^{++})$  for upper limits, against the measured  $N_{\text{HI}}$  value for the COS-Halos sample. The dotted/dashed lines demarcate four regions of the plot: (A)  $N_{\text{HI}} \leq 10^{16} \text{ cm}^{-2}$  and  $N_{\text{Low}} \geq 10^{12.3} \text{ cm}^{-2}$ , where the gas highly ionized; (B)  $N_{\text{HI}} \geq 10^{16} \text{ cm}^{-2}$  and  $N_{\text{Low}} \geq 10^{12.3} \text{ cm}^{-2}$ , where the majority of positive detections for low ions lie; and (C)  $N_{\text{HI}} \leq 10^{16} \text{ cm}^{-2}$  and  $N_{\text{Low}} < 10^{12.3} \text{ cm}^{-2}$  where the majority of non-detections are located; and (D)  $N_{\text{HI}} \geq 10^{16} \text{ cm}^{-2}$  and  $N_{\text{Low}} < 10^{12.3} \text{ cm}^{-2}$ , a region that would indicate metal-poor gas. This region is unoccupied, suggesting the CGM of  $L^*$  galaxies is significantly enriched. Another key point shown by this figure is that low ion column density is significantly coupled to H I column density, with detections essentially requiring a non-negligible opacity at the H I Lyman limit.

(A color version of this figure is available in the online journal.)

Despite the cool temperature ( $T < 10^5 \text{ K}$ ), we have argued that the gas is predominantly ionized based on the relative abundances of the intermediate and low ions (Figure 10). This conclusion depends, in part, on the assertion that the low ion gas arises in the same regions as the intermediate ion gas. Direct

inspection of the line profiles (Figure 3) and comparisons of the profile fits (Figure 11) support this conclusion. The dominance of the intermediate ions then implies that the hydrogen gas is at least 50% ionized and more likely  $>90\%$ . One can limit the degree of ionization through an additional comparison with the high-ion states (e.g., Si IV, C IV). Although these transitions have poorer data quality, they generally indicate that the majority of cool gas is not very highly ionized. Of course, this comparison ignores the nearly ubiquitous  $\text{O}^{+5}$  gas present in SF galaxies, which must be very highly ionized. A direct implication, to be explored further in future work, is that the cool CGM traces a distinct gas from that bearing the  $\text{O}^{+5}$  absorption.

Our survey also demonstrates that the cool CGM of  $L^*$  galaxies hosts a large mass reservoir of metals and gas. Figure 14 presents the minimum metal column density,  $N_{\text{min}}(\text{O})$ , for each system against impact parameter, with the former defined as follows. For each system, we consider the positive detections of the low and intermediate ions (values and lower limits) and convert these to a pseudo-oxygen ionic column density, assuming solar relative abundances, i.e., the  $N_{\text{min}}(\text{O})$  value for  $N(\text{Si}^{++}) = 10^{13.5} \text{ cm}^{-2}$  is  $N_{\text{min}}(\text{O}) = 10^{14.68} \text{ cm}^{-2}$ . These are *minimum* values because (1) many of the lines are saturated and (2) these columns are derived from a single ionization state, such that we assume the ion fraction of the given species is one. For each system, we take the maximum  $N_{\text{min}}(\text{O})$  value recorded for all detected ions, as presented in Figure 14. The measurements are dominated by intermediate ionization states, primarily  $\text{Si}^{++}$ ,  $\text{C}^{++}$ , and  $\text{N}^{+}$  with only two values derived from a low ion.<sup>15</sup> The  $N_{\text{min}}(\text{O})$  values are large, frequently exceeding  $10^{15} \text{ cm}^{-2}$  with a median of  $10^{14.6} \text{ cm}^{-2}$  for the full sample. The value is actually comparable to the median  $N_{\text{HI}}$  of the sample

<sup>15</sup> To be conservative, for this analysis we have ignored measurements derived from Si III  $\lambda 989$  owing to concerns that it is blended with Si III  $\lambda 989$ . This has only a minor effect on the results, however.

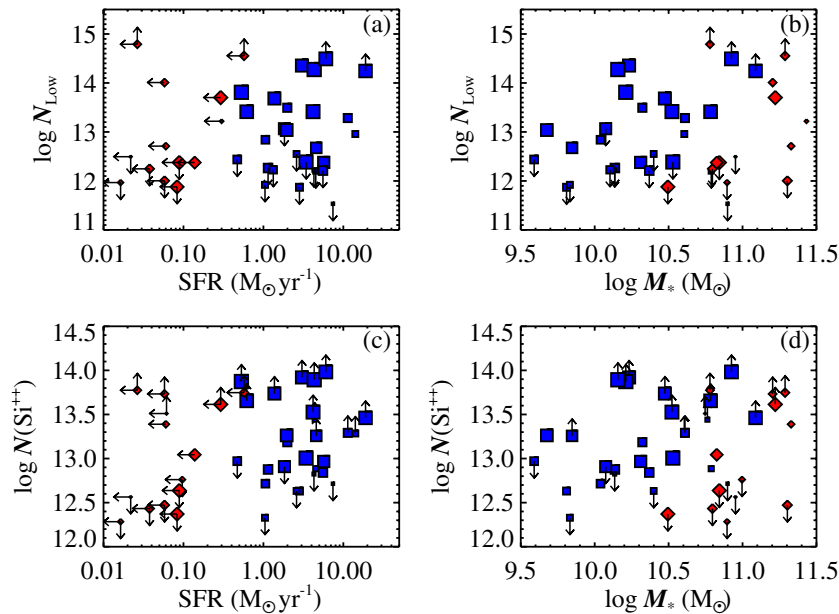


**Figure 6.** Panels (a) and (b) show the low ion column density against the galaxy properties SFR and stellar mass. Regarding SFR, there is little correlation between the two measurements; the only notable result is a possible bimodality in the  $N_{\text{Low}}$  values for the non-SF population. In terms of stellar mass, there are two key results: (1) an apparent trend of increasing  $N_{\text{Low}}$  with increasing  $M_*$  and (2) a nearly perfect separation between the measurements of the SF and non-SF populations. In all panels, the symbol size is inversely proportional to the impact parameter. The lower panels (c) and (d) show the  $\text{Si}^{++}$  column density against the galaxy properties. Again, we note no obvious trend with SFR but observe a strong dependence with  $M_*$ .

(A color version of this figure is available in the online journal.)



**Table 5**  
Covering Fraction (EW)

Ion	Sample	$N_{\text{TOT}}$	$\text{EW}_{\text{limit}}$ (mÅ)	$C_f[0, 75]$	$C_f[75, 160]$	$C_f[0, 160]$
Low ion transitions						
Mg II 2796	All	39	100	$68^{+11}_{-11}$	$52^{+10}_{-22}$	$59^{+8}_{-15}$
Mg II 2796	$\text{sSFR} < 10^{-11} \text{ yr}^{-1}$	13	100	$30^{+20}_{-20}$	$65^{+15}_{-26}$	$54^{+13}_{-20}$
Mg II 2796	$\text{sSFR} \geq 10^{-11} \text{ yr}^{-1}$	26	100	$81^{+11}_{-11}$	$43^{+13}_{-25}$	$61^{+9}_{-17}$
Mg II 2796	$M_* < 10^{10.5} M_{\odot}$	17	100	$72^{+15}_{-15}$	$35^{+15}_{-31}$	$53^{+12}_{-23}$
Mg II 2796	$M_* \geq 10^{10.5} M_{\odot}$	22	100	$61^{+16}_{-16}$	$63^{+12}_{-19}$	$63^{+10}_{-15}$
Si II 1260	All	39	150	$57^{+13}_{-13}$	$40^{+10}_{-24}$	$46^{+8}_{-18}$
Si II 1260	$\text{sSFR} < 10^{-11} \text{ yr}^{-1}$	14	150	$30^{+20}_{-20}$	$50^{+15}_{-32}$	$43^{+13}_{-25}$
Si II 1260	$\text{sSFR} \geq 10^{-11} \text{ yr}^{-1}$	25	150	$68^{+14}_{-14}$	$34^{+12}_{-23}$	$48^{+10}_{-17}$
Si II 1260	$M_* < 10^{10.5} M_{\odot}$	17	150	$44^{+17}_{-17}$	$32^{+14}_{-28}$	$36^{+11}_{-21}$
Si II 1260	$M_* \geq 10^{10.5} M_{\odot}$	22	150	$69^{+16}_{-16}$	$47^{+12}_{-24}$	$54^{+10}_{-19}$
C II 1036	All	39	80	$63^{+12}_{-12}$	$48^{+10}_{-17}$	$54^{+8}_{-13}$
C II 1036	$\text{sSFR} < 10^{-11} \text{ yr}^{-1}$	14	80	$37^{+24}_{-24}$	$54^{+14}_{-23}$	$50^{+13}_{-19}$
C II 1036	$\text{sSFR} \geq 10^{-11} \text{ yr}^{-1}$	25	80	$71^{+13}_{-13}$	$43^{+13}_{-19}$	$56^{+10}_{-14}$
C II 1036	$M_* < 10^{10.5} M_{\odot}$	17	80	$56^{+17}_{-17}$	$41^{+15}_{-23}$	$47^{+12}_{-17}$
C II 1036	$M_* \geq 10^{10.5} M_{\odot}$	22	80	$69^{+16}_{-16}$	$53^{+12}_{-19}$	$59^{+10}_{-15}$
Intermediate ion transitions						
C III 977	All	25	100	$88^{+8}_{-18}$	$82^{+10}_{-19}$	$87^{+7}_{-16}$
C III 977	$\text{sSFR} < 10^{-11} \text{ yr}^{-1}$	11	100	$70^{+20}_{-42}$	$81^{+13}_{-29}$	$79^{+11}_{-31}$
C III 977	$\text{sSFR} \geq 10^{-11} \text{ yr}^{-1}$	14	100	$94^{+6}_{-6}$	$79^{+15}_{-15}$	$90^{+7}_{-7}$
C III 977	$M_* < 10^{10.5} M_{\odot}$	8	100	$70^{+20}_{-20}$	$90^{+10}_{-10}$	$83^{+12}_{-12}$
C III 977	$M_* \geq 10^{10.5} M_{\odot}$	17	100	$94^{+6}_{-23}$	$75^{+13}_{-25}$	$86^{+8}_{-21}$
Si III 1206	All	41	100	$86^{+8}_{-15}$	$62^{+10}_{-22}$	$73^{+7}_{-17}$
Si III 1206	$\text{sSFR} < 10^{-11} \text{ yr}^{-1}$	14	100	$50^{+22}_{-22}$	$59^{+15}_{-24}$	$57^{+13}_{-20}$
Si III 1206	$\text{sSFR} \geq 10^{-11} \text{ yr}^{-1}$	27	100	$96^{+4}_{-15}$	$63^{+12}_{-26}$	$80^{+7}_{-19}$
Si III 1206	$M_* < 10^{10.5} M_{\odot}$	18	100	$85^{+11}_{-23}$	$55^{+16}_{-35}$	$71^{+10}_{-27}$
Si III 1206	$M_* \geq 10^{10.5} M_{\odot}$	23	100	$83^{+12}_{-12}$	$66^{+12}_{-18}$	$73^{+9}_{-14}$
High-ion transitions						
Si IV 1393	All	31	100	$96^{+4}_{-72}$	$64^{+10}_{-52}$	$77^{+7}_{-58}$
Si IV 1393	$\text{sSFR} < 10^{-11} \text{ yr}^{-1}$	11	100	$88^{+12}_{-74}$	$61^{+16}_{-48}$	$71^{+13}_{-55}$
Si IV 1393	$\text{sSFR} \geq 10^{-11} \text{ yr}^{-1}$	20	100	$94^{+6}_{-72}$	$65^{+13}_{-57}$	$79^{+9}_{-62}$
Si IV 1393	$M_* < 10^{10.5} M_{\odot}$	14	100	$92^{+8}_{-84}$	$55^{+16}_{-51}$	$70^{+12}_{-63}$
Si IV 1393	$M_* \geq 10^{10.5} M_{\odot}$	17	100	$93^{+7}_{-62}$	$71^{+13}_{-55}$	$81^{+9}_{-56}$
Other						
H I 1215	All	42	200	$91^{+6}_{-6}$	$87^{+6}_{-6}$	$90^{+5}_{-5}$
H I 1215	$\text{sSFR} < 10^{-11} \text{ yr}^{-1}$	15	200	$70^{+20}_{-20}$	$71^{+13}_{-13}$	$72^{+11}_{-11}$
H I 1215	$\text{sSFR} \geq 10^{-11} \text{ yr}^{-1}$	27	200	$96^{+4}_{-4}$	$97^{+3}_{-3}$	$98^{+2}_{-2}$
H I 1215	$M_* < 10^{10.5} M_{\odot}$	18	200	$83^{+12}_{-12}$	$96^{+4}_{-4}$	$92^{+6}_{-6}$
H I 1215	$M_* \geq 10^{10.5} M_{\odot}$	24	200	$94^{+6}_{-6}$	$79^{+10}_{-10}$	$86^{+7}_{-7}$
O VI 1031	All	33	100	$83^{+9}_{-9}$	$73^{+10}_{-15}$	$78^{+7}_{-10}$
O VI 1031	$\text{sSFR} < 10^{-11} \text{ yr}^{-1}$	9	100	$37^{+24}_{-24}$	$50^{+19}_{-32}$	$45^{+16}_{-25}$
O VI 1031	$\text{sSFR} \geq 10^{-11} \text{ yr}^{-1}$	24	100	$96^{+4}_{-4}$	$82^{+10}_{-10}$	$90^{+6}_{-6}$
O VI 1031	$M_* < 10^{10.5} M_{\odot}$	16	100	$81^{+13}_{-13}$	$95^{+5}_{-5}$	$91^{+6}_{-6}$
O VI 1031	$M_* \geq 10^{10.5} M_{\odot}$	17	100	$81^{+13}_{-13}$	$50^{+15}_{-24}$	$64^{+11}_{-17}$

**Notes.** A table of covering fractions relating to the equivalent width measured for selected transitions, given for various ranges in impact parameter (in kpc). These values are shown as percentages in the last three columns along with their associated errors. The error reported in  $C_f$ , which follows a standard binomial Wilson score, accounts for this uncertainty by calculating the 68% confidence interval assuming that upper limits above the threshold do not satisfy it. We divide the sample into several subsamples (Column 2) based on sSFR and mass. The total number of galaxies whose COS spectra cover the transition in question in each subsample is given in Column 2. The values for H I and O VI were derived from the measurements presented in J. Tumlinson et al. (in preparation) and Tumlinson et al. (2011), respectively.

**Table 6**  
Covering Fraction (Column Density)

Ion	Sample	$N_{\text{TOT}}$	$\log N_{\text{limit}}$	$C_f[0, 75]$	$C_f[75, 160]$	$C_f[0, 160]$
Low ion transitions						
Mg II	All	40	12.50	$68^{+11}_{-18}$	$42^{+10}_{-14}$	$52^{+8}_{-13}$
Mg II	$\text{sSFR} < 10^{-11} \text{ yr}^{-1}$	13	12.50	$30^{+20}_{-20}$	$55^{+16}_{-16}$	$46^{+13}_{-13}$
Mg II	$\text{sSFR} \geq 10^{-11} \text{ yr}^{-1}$	27	12.50	$81^{+11}_{-20}$	$34^{+12}_{-17}$	$55^{+9}_{-17}$
Mg II	$M_* < 10^{10.5} M_{\odot}$	18	12.50	$72^{+15}_{-27}$	$23^{+12}_{-19}$	$45^{+11}_{-21}$
Mg II	$M_* \geq 10^{10.5} M_{\odot}$	22	12.50	$61^{+16}_{-16}$	$57^{+13}_{-13}$	$59^{+10}_{-10}$
Si II	All	42	13.00	$74^{+11}_{-36}$	$50^{+10}_{-31}$	$59^{+7}_{-31}$
Si II	$\text{sSFR} < 10^{-11} \text{ yr}^{-1}$	15	13.00	$30^{+20}_{-20}$	$54^{+14}_{-31}$	$47^{+12}_{-24}$
Si II	$\text{sSFR} \geq 10^{-11} \text{ yr}^{-1}$	27	13.00	$88^{+8}_{-44}$	$47^{+12}_{-35}$	$66^{+9}_{-38}$
Si II	$M_* < 10^{10.5} M_{\odot}$	18	13.00	$72^{+15}_{-49}$	$50^{+15}_{-46}$	$61^{+11}_{-46}$
Si II	$M_* \geq 10^{10.5} M_{\odot}$	24	13.00	$72^{+15}_{-27}$	$50^{+12}_{-23}$	$58^{+10}_{-22}$
C II	All	42	13.75	$79^{+10}_{-29}$	$54^{+10}_{-21}$	$64^{+7}_{-22}$
C II	$\text{sSFR} < 10^{-11} \text{ yr}^{-1}$	15	13.75	$50^{+22}_{-22}$	$54^{+14}_{-23}$	$53^{+12}_{-19}$
C II	$\text{sSFR} \geq 10^{-11} \text{ yr}^{-1}$	27	13.75	$88^{+8}_{-36}$	$53^{+12}_{-25}$	$70^{+9}_{-27}$
C II	$M_* < 10^{10.5} M_{\odot}$	18	13.75	$83^{+12}_{-50}$	$41^{+15}_{-23}$	$61^{+11}_{-32}$
C II	$M_* \geq 10^{10.5} M_{\odot}$	24	13.75	$72^{+15}_{-15}$	$62^{+12}_{-24}$	$66^{+9}_{-18}$
Intermediate ion transitions						
C III	All	25	13.00	$96^{+4}_{-28}$	$90^{+7}_{-32}$	$94^{+4}_{-28}$
C III	$\text{sSFR} < 10^{-11} \text{ yr}^{-1}$	11	13.00	$90^{+10}_{-62}$	$94^{+6}_{-41}$	$96^{+4}_{-47}$
C III	$\text{sSFR} \geq 10^{-11} \text{ yr}^{-1}$	14	13.00	$94^{+6}_{-6}$	$81^{+13}_{-29}$	$90^{+7}_{-16}$
C III	$M_* < 10^{10.5} M_{\odot}$	7	13.00	$88^{+12}_{-49}$	$90^{+10}_{-10}$	$94^{+6}_{-26}$
C III	$M_* \geq 10^{10.5} M_{\odot}$	18	13.00	$94^{+6}_{-23}$	$86^{+10}_{-42}$	$92^{+6}_{-31}$
Si III	All	40	12.75	$85^{+8}_{-15}$	$62^{+10}_{-22}$	$72^{+7}_{-17}$
Si III	$\text{sSFR} < 10^{-11} \text{ yr}^{-1}$	14	12.75	$50^{+22}_{-22}$	$59^{+15}_{-24}$	$57^{+13}_{-20}$
Si III	$\text{sSFR} \geq 10^{-11} \text{ yr}^{-1}$	26	12.75	$96^{+4}_{-16}$	$63^{+12}_{-26}$	$80^{+8}_{-20}$
Si III	$M_* < 10^{10.5} M_{\odot}$	17	12.75	$83^{+12}_{-26}$	$55^{+16}_{-35}$	$69^{+11}_{-28}$
Si III	$M_* \geq 10^{10.5} M_{\odot}$	23	12.75	$83^{+12}_{-12}$	$66^{+12}_{-18}$	$73^{+9}_{-14}$
High-ion transitions						
Si IV	All	32	13.25	$88^{+9}_{-64}$	$57^{+10}_{-45}$	$68^{+8}_{-50}$
Si IV	$\text{sSFR} < 10^{-11} \text{ yr}^{-1}$	12	13.25	$63^{+24}_{-49}$	$55^{+16}_{-43}$	$58^{+14}_{-43}$
Si IV	$\text{sSFR} \geq 10^{-11} \text{ yr}^{-1}$	20	13.25	$94^{+6}_{-72}$	$58^{+14}_{-49}$	$74^{+9}_{-57}$
Si IV	$M_* < 10^{10.5} M_{\odot}$	14	13.25	$75^{+17}_{-67}$	$45^{+16}_{-41}$	$57^{+13}_{-49}$
Si IV	$M_* \geq 10^{10.5} M_{\odot}$	18	13.25	$93^{+7}_{-62}$	$65^{+13}_{-51}$	$76^{+10}_{-53}$
Other						
H I	All	43	13.50	$91^{+6}_{-6}$	$88^{+6}_{-6}$	$90^{+4}_{-4}$
H I	$\text{sSFR} < 10^{-11} \text{ yr}^{-1}$	16	13.50	$70^{+20}_{-20}$	$73^{+12}_{-12}$	$74^{+11}_{-11}$
H I	$\text{sSFR} \geq 10^{-11} \text{ yr}^{-1}$	27	13.50	$96^{+4}_{-4}$	$97^{+3}_{-3}$	$98^{+2}_{-2}$
H I	$M_* < 10^{10.5} M_{\odot}$	18	13.50	$83^{+12}_{-12}$	$96^{+4}_{-4}$	$92^{+6}_{-6}$
H I	$M_* \geq 10^{10.5} M_{\odot}$	25	13.50	$94^{+6}_{-6}$	$81^{+9}_{-9}$	$87^{+7}_{-7}$
O VI	All	40	14.15	$83^{+9}_{-9}$	$69^{+9}_{-17}$	$74^{+7}_{-12}$
O VI	$\text{sSFR} < 10^{-11} \text{ yr}^{-1}$	14	14.15	$37^{+24}_{-24}$	$46^{+14}_{-30}$	$43^{+13}_{-25}$
O VI	$\text{sSFR} \geq 10^{-11} \text{ yr}^{-1}$	26	14.15	$96^{+4}_{-4}$	$84^{+9}_{-9}$	$91^{+5}_{-5}$
O VI	$M_* < 10^{10.5} M_{\odot}$	17	14.15	$81^{+13}_{-13}$	$96^{+4}_{-4}$	$92^{+6}_{-6}$
O VI	$M_* \geq 10^{10.5} M_{\odot}$	23	14.15	$81^{+13}_{-13}$	$50^{+12}_{-23}$	$60^{+10}_{-18}$

**Notes.** A table of covering fractions relating to the column density measured for selected transitions, given for various ranges in impact parameter (in kpc). These values are shown as percentages in the last three columns along with their associated errors. Here, the error reported in  $C_f$ , which follows a standard binomial Wilson score, treats upper limits above the threshold as detections and considers lower limits below the threshold as satisfying it. In this case,  $C_f$  values are maximal, aside from Poisson error. We divide the sample into several subsamples (Column 2) based on sSFR and mass. The total number of galaxies whose COS spectra cover the transition in question in each subsample is given in Column 2. The values for H I and O VI were derived from the measurements presented in J. Tumlinson et al. (in preparation) and Tumlinson et al. (2011), respectively.

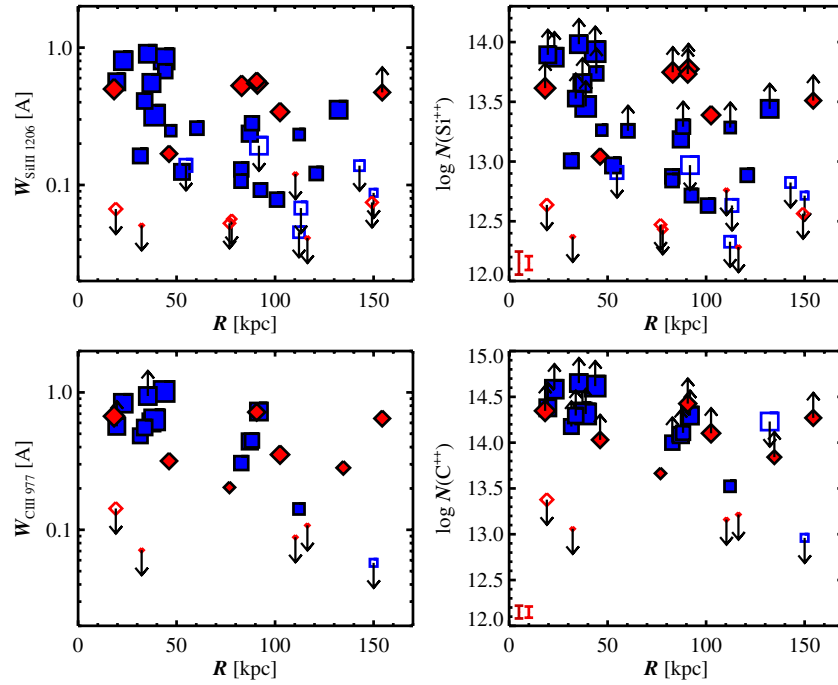


**Figure 7.** Similar to Figure 4, but for the intermediate ions of Si<sup>++</sup> (upper) and C<sup>++</sup> (lower). There is a high incidence (>80%) of detections for these ions, especially within the SF population. There is also a very significant anti-correlation (>99% c.l.) between intermediate ion absorption strength and impact parameter. Despite the lower incidence of positive detections among the non-SF galaxies, the detected values match or even exceed the typical values of SF galaxies.

(A color version of this figure is available in the online journal.)

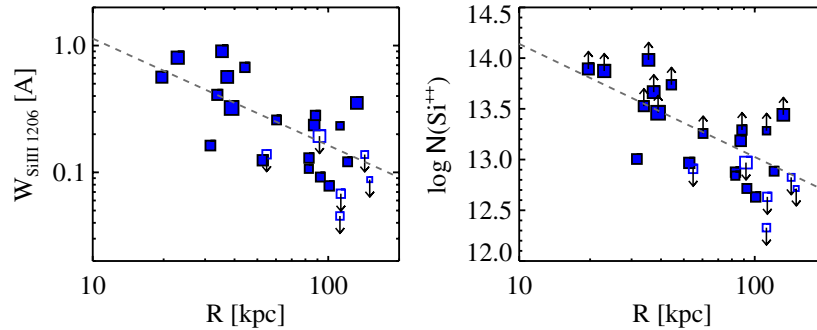


**Figure 8.** Fitted equivalent widths and column densities for Si<sup>++</sup> as a function of impact parameter, restricted to the SF galaxies. If we (incorrectly) treat all measurements as values, we measure power-law exponents for the variation in  $W_r$  and  $N$  with  $R$ :  $\alpha_W = -0.84 \pm 0.24$  and  $\alpha_N = -1.11 \pm 0.29$ . A proper treatment of limits would only steepen these slopes.

(A color version of this figure is available in the online journal.)

( $10^{15.4} \text{ cm}^{-2}$ ). This result is not surprising if we simply consider that the gas is predominantly ionized.

Independent of the direct H I measurements, if the gas has a solar metallicity or lower then the median  $N_{\min}(\text{O})$  value implies a total hydrogen column of  $N_{\text{H}} > 10^{18} \text{ cm}^{-2}$ . We stress again that this is a conservative lower limit because it is derived from a single ionization state and many of the measured ionic column densities are lower limits because of line saturation. As important, the average  $N_{\min}(\text{O})$  value is nearly  $10\times$  larger than the median. The implied total gas mass for the cool CGM, therefore, is at least

$$M_{\text{CGM}}^{\text{cool}} > 10^9 \left( \frac{R}{160 \text{ kpc}} \right)^2 \left( \frac{N_{\text{H}}}{10^{18} \text{ cm}^{-2}} \right) \left( \frac{Z_{\odot}}{Z} \right) M_{\odot}. \quad (3)$$

In this equation, we have taken the mass as a surface area times a median column density, such that  $M_{\text{CGM}} = 1.4\pi R^2 \tilde{N}_{\text{H}} m_p$ . Here,  $\tilde{N}_{\text{H}}$  is the median total hydrogen column (which we assume has a

covering fraction of  $\sim 100\%$ , consistent with the data),  $m_p$  is the mass of a proton, and the factor of 1.4 corrects for helium and metals. For reference,  $N_{\text{H}} = 10^{18} \text{ cm}^{-2}$ , which is the median hydrogen column computed at solar metallicity for a single ionization state, corresponds to  $M_{\text{H}} = 10^{3.9} M_{\odot} \text{ kpc}^{-2}$ . Future work will improve this very conservative lower limit through detailed ionization modeling of the gas (J. K. Werk et al., in preparation), and we expect the value to rise by at least one order of magnitude.

Figure 14 also plots the O<sup>+5</sup> column densities for these systems, connected to the  $N_{\min}(\text{O})$  values by a dashed gray line. It is difficult to identify any particular correlation between the two sets of measurements. The  $N(\text{O}^{+5})$  values occupy a relatively narrow range of values and tend to be lower than the  $N_{\min}(\text{O})$  estimates. In this respect, the figure suggests that the lower ionization states dominate the metal reservoir. Unfortunately, this hypothesis is difficult to test because the physical origin (e.g., its ionization mechanism) of O<sup>+5</sup> is unknown and corrections for ionization may be very large.

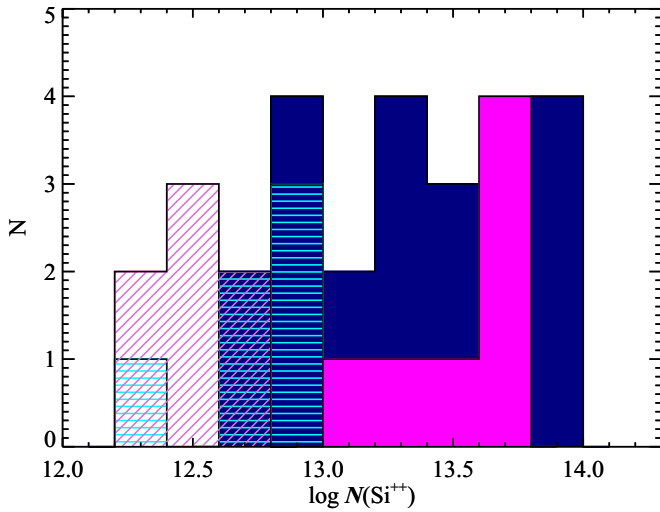


**Figure 9.** Histogram of  $\text{Si}^{++}$  column densities for the SF galaxies (solid blue shows detections and lower limits; cyan hatches are upper limits) and non-SF galaxies (solid magenta shows detections and lower limits; pink hatches are upper limits). Whereas the values for the SF galaxies exhibit a relatively uniform distribution of values, the non-SF galaxies have a bimodal distribution of positive detections and upper limits. This implies that the CGM of the non-SF galaxies has a bimodal behavior either locally (e.g., a patchy distribution around each galaxy) and/or globally (the CGM exists around some but not all non-SF galaxies).

(A color version of this figure is available in the online journal.)

Indeed, it is generally accepted that the ionization fraction of  $\text{O}^{+5}$  does not exceed 0.2, so in this respect the values are likely to be scaled up by a factor of five if they are to be compared to the total oxygen (for consistency, we have left  $f = 1.0$  for the low and intermediate ions).

Another trend emphasized in the previous section (e.g., Section 4.2) and also revealed by Figure 14 is that the metal

column densities decrease with increasing impact parameter. This is true for both the detection rate and the measured values. We conclude that the metal surface density of the CGM decreases with radius, both in the cool gas traced by the transitions analyzed in this paper and the highly ionized gas traced by  $\text{O}^{+5}$ . Future work will study whether or not this trend is driven by a decline in metallicity, total surface density, or both (J. K. Werk et al., in preparation).

Despite the preponderance of positive detections, there are 11 systems without significant absorption from low or intermediate ions; each is shown with an open symbol at an arbitrary value of  $10^{13.5} \text{ cm}^{-2}$  in Figure 14. Nearly all of these systems also exhibit  $N_{\text{H I}} < 10^{14.5} \text{ cm}^{-2}$ . The majority of cases are associated with quiescent galaxies and none of these show  $\text{O}^{+5}$  absorption. These non-detections arise either because of a “hole” in the CGM of these galaxies or because the galaxy lacks a CGM altogether. In contrast, all but one of the SF galaxies exhibit a positive  $\text{O}^{+5}$  detection and strong H I absorption. This suggests the cool CGM of SF galaxies is “patchy,” corresponding physically to a non-unity volume filling factor. This is in contrast with the highly ionized CGM traced by  $\text{O}^{+5}$ .

Such a patchy characteristic is further supported by the observed distribution of equivalent widths for low ion gas at large impact parameters ( $R > 70 \text{ kpc}$ ; Figure 4). Considering both detections and limits, one observes a very wide dispersion in the measurements (at least an order of magnitude) that is uniformly distributed. This occurs despite the fact that most of the sightlines show strong H I and  $\text{O}^{+5}$  absorption (Figure 12). We conclude that the CGM has a patchy distribution of low ion gas.

The kinematics of the gas offer additional insight into the nature of the cool CGM. In J. Tumlinson et al. (in preparation), we compare the gas kinematics of the H I gas to estimates of the escape velocity and argued that the majority of that material is not escaping. Figure 15 presents a similar analysis, based

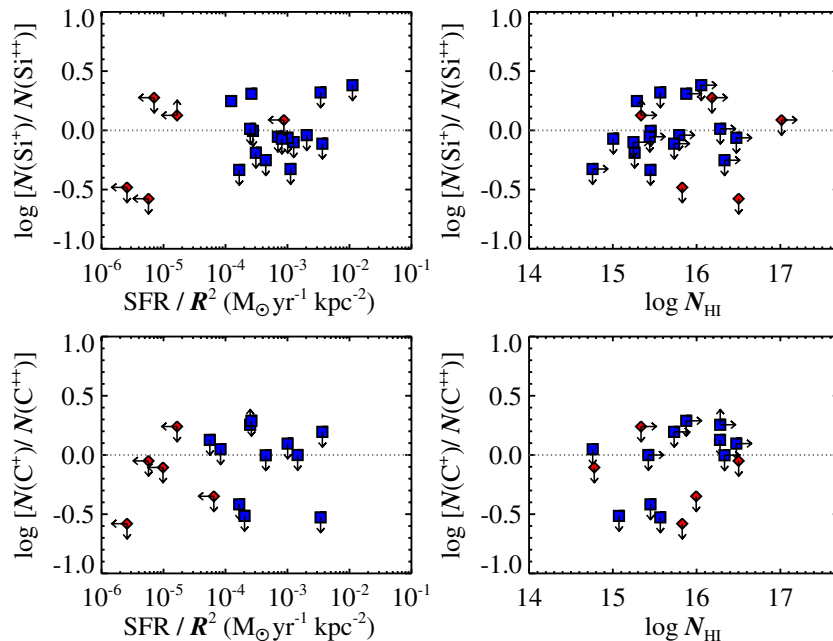


**Figure 10.** Comparison of the low ( $\text{Si}^+$ ,  $\text{C}^+$ ) and intermediate ( $\text{Si}^{++}$ ,  $\text{C}^{++}$ ) ionic column density ratios against a crude estimate of the ionizing flux from SF galaxies ( $\text{SFR}/R^2$ ) and the H I column densities of the gas  $N_{\text{H I}}$ . The principal result is that the ratios are low:  $N(\text{Si}^+)/N(\text{Si}^{++})$  and  $N(\text{C}^+)/N(\text{C}^{++})$  are less than one for the vast majority of systems and nearly all are consistent with falling below unity. This result indicates that the CGM gas of  $L^*$  galaxies is highly ionized. Note that 22(27) systems are not plotted for  $\text{Si}(\text{C})$  because both species are lower limits or upper limits and/or there was no coverage of C III  $\lambda 977$  in the data.

(A color version of this figure is available in the online journal.)

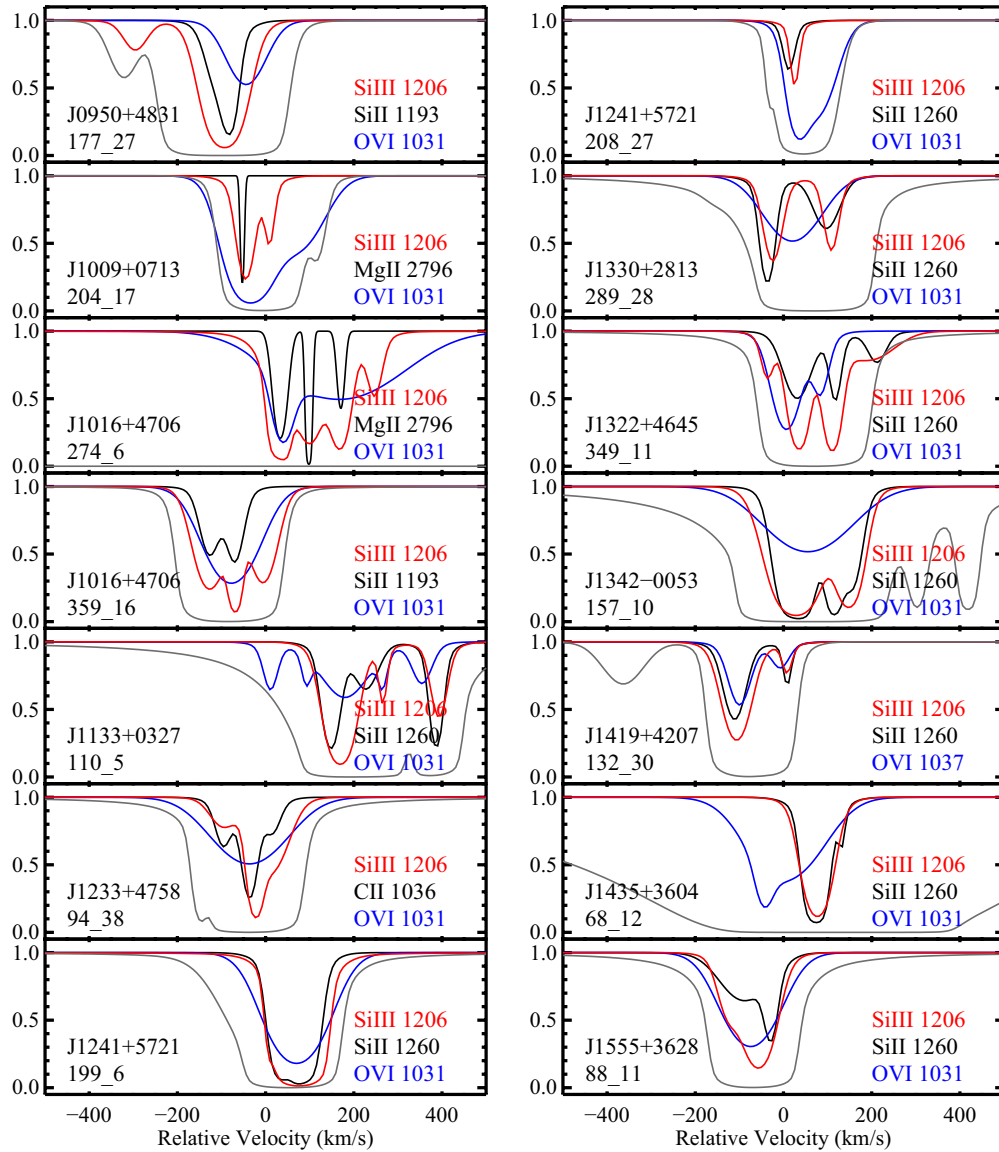


**Figure 11.** Comparison of the normalized profile fits for the low (black), intermediate (red), and high ( $O^{+5}$ , blue) ion transitions for selected systems where there is a strong detection of each. We also show the profile fits to the  $H\text{ I } \text{Ly}\alpha$  line (saturated in each of these cases) in dark gray for reference.

(A color version of this figure is available in the online journal.)

on the line-profile fits for the metals in the cool CGM. Two results should be emphasized from the figure. First, the dominant gas components (solid points) have a velocity dispersion about systemic of  $\sigma \approx 85 \text{ km s}^{-1}$ . Wavelength error and uncertainty in the galaxy redshifts contribute to this dispersion, but only on the order of 10%–20%. Therefore, the gas has significant motions relative to the galaxy. These motions, however, are consistent with the velocity dispersion predicted for the dark matter halos hosting  $L^*$  galaxies and we conclude that the majority of gas is confined to the system. Second, the line-profiles tend to span only 50–100  $\text{km s}^{-1}$ ; only a few examples show motions in excess of 200  $\text{km s}^{-1}$ . Similar to J. Tumlinson et al. (in preparation), we conclude the cool CGM is bound to the galaxy.

Another aspect of the kinematics revealed in Figure 15 is that a majority of galaxies show metal-line profiles that span the systemic velocity. This appears to contrast with previous work on  $\text{Mg II}$  kinematics, where the profiles have tended to lie on only

one side of systemic (Steidel et al. 2002; Kacprzak et al. 2010). However, this difference is most likely the result of sample selection effects related to galaxy disk orientation. Steidel et al. (2002) selected galaxies to have edge-on orientation, while Kacprzak et al. (2010) tended to avoid face-on galaxies. Thus, the offsets are a natural expectation of disk-like rotation, and our results remain consistent with those of Steidel et al. (2002) and Kacprzak et al. (2010). Our results do differ from models for accreting cool gas which predict the material should have high angular momentum and therefore show absorption with large velocity offset to one side of systemic (Stewart et al. 2011).

## 6. SUMMARY AND CONCLUSIONS

In this paper, we have presented the equivalent width, column density measurements, and line profile fits for low and intermediate ionization states of the CGM surrounding 44 low- $z$ ,  $L \approx L^*$  galaxies drawn from the COS-Halos survey.



**Table 7**  
Absorption Strength Statistics

Ion	Sample	$\tilde{W}^a$ [0, 75]	$\tilde{W}^a$ [75, 160]	$\tilde{W}^a$ [0, 160]	$\langle W \rangle^b$ [0, 75]	$\langle W \rangle^b$ [75, 160]	$\langle W \rangle^b$ [0, 160]	$\log \tilde{N}^c$ [0, 75]	$\log \tilde{N}^c$ [75, 160]	$\log \tilde{N}^c$ [0, 160]	$\langle \log N \rangle^d$ [0, 75]	$\langle \log N \rangle^d$ [75, 160]	$\langle \log N \rangle^d$ [0, 160]
Low ion transitions													
Mg II 2796	All	314	101	127	482 ± 463	245 ± 333	343 ± 403	13.1	12.4	12.7	13.1 ± 0.67	12.6 ± 0.70	12.8 ± 0.72
Mg II 2796	sSFR < 10 <sup>-11</sup> yr <sup>-1</sup>	86	180	111	249 ± 372	407 ± 472	358 ± 435	12.4	12.7	12.5	12.6 ± 0.73	12.9 ± 0.83	12.8 ± 0.79
Mg II 2796	sSFR ≥ 10 <sup>-11</sup> yr <sup>-1</sup>	454	67	203	560 ± 478	142 ± 143	335 ± 395	13.3	12.3	13.0	13.3 ± 0.58	12.5 ± 0.58	12.8 ± 0.70
Mg II 2796	$M_* < 10^{10.5} M_\odot$	454	66	101	499 ± 486	99 ± 105	287 ± 389	13.1	12.3	12.4	13.1 ± 0.71	12.3 ± 0.41	12.7 ± 0.68
Mg II 2796	$M_* \geq 10^{10.5} M_\odot$	314	227	246	466 ± 472	339 ± 395	385 ± 418	13.3	13.0	13.0	13.1 ± 0.68	12.8 ± 0.80	12.9 ± 0.75
Si II 1260	All	292	115	142	300 ± 231	179 ± 169	223 ± 200	13.4	13.0	13.2	13.5 ± 0.59	13.1 ± 0.58	13.3 ± 0.60
Si II 1260	sSFR < 10 <sup>-11</sup> yr <sup>-1</sup>	70	200	133	169 ± 208	261 ± 239	235 ± 226	12.7	13.0	13.0	13.0 ± 0.49	13.3 ± 0.78	13.2 ± 0.72
Si II 1260	sSFR ≥ 10 <sup>-11</sup> yr <sup>-1</sup>	297	114	145	353 ± 228	125 ± 67	216 ± 187	13.4	13.0	13.2	13.6 ± 0.54	13.0 ± 0.33	13.3 ± 0.55
Si II 1260	$M_* < 10^{10.5} M_\odot$	142	115	134	282 ± 229	119 ± 74	186 ± 172	13.2	13.0	13.1	13.5 ± 0.59	12.9 ± 0.34	13.2 ± 0.54
Si II 1260	$M_* \geq 10^{10.5} M_\odot$	292	133	200	319 ± 250	220 ± 203	251 ± 218	13.4	13.0	13.3	13.5 ± 0.64	13.2 ± 0.67	13.3 ± 0.65
C II 1036	All	204	80	99	240 ± 193	132 ± 125	171 ± 159	14.3	14.0	14.1	14.3 ± 0.52	14.0 ± 0.46	14.1 ± 0.50
C II 1036	sSFR < 10 <sup>-11</sup> yr <sup>-1</sup>	55	99	99	191 ± 238	182 ± 167	184 ± 174	14.1	13.9	13.9	14.0 ± 0.62	14.0 ± 0.59	14.0 ± 0.58
C II 1036	sSFR ≥ 10 <sup>-11</sup> yr <sup>-1</sup>	204	59	132	253 ± 190	93 ± 60	164 ± 154	14.4	14.0	14.2	14.4 ± 0.46	13.9 ± 0.36	14.1 ± 0.46
C II 1036	$M_* < 10^{10.5} M_\odot$	150	50	79	199 ± 167	92 ± 64	136 ± 125	14.3	13.7	14.0	14.2 ± 0.51	13.9 ± 0.38	14.0 ± 0.46
C II 1036	$M_* \geq 10^{10.5} M_\odot$	258	99	99	280 ± 222	160 ± 149	198 ± 179	14.5	14.1	14.1	14.3 ± 0.54	14.0 ± 0.51	14.1 ± 0.53
Intermediate ion transitions													
C III 977	All	605	306	446	570 ± 290	347 ± 236	454 ± 281	14.3	14.1	14.2	14.2 ± 0.49	13.8 ± 0.47	14.0 ± 0.50
C III 977	sSFR < 10 <sup>-11</sup> yr <sup>-1</sup>	317	283	283	301 ± 268	343 ± 251	327 ± 244	14.0	13.8	13.8	13.7 ± 0.59	13.8 ± 0.50	13.8 ± 0.50
C III 977	sSFR ≥ 10 <sup>-11</sup> yr <sup>-1</sup>	631	440	567	704 ± 198	353 ± 240	554 ± 276	14.4	14.1	14.3	14.4 ± 0.17	13.9 ± 0.48	14.2 ± 0.44
C III 977	$M_* < 10^{10.5} M_\odot$	834	440	567	622 ± 411	403 ± 247	513 ± 335	14.6	14.1	14.3	14.2 ± 0.74	14.0 ± 0.33	14.1 ± 0.54
C III 977	$M_* \geq 10^{10.5} M_\odot$	605	283	446	543 ± 240	323 ± 241	427 ± 259	14.3	14.1	14.2	14.2 ± 0.37	13.8 ± 0.52	14.0 ± 0.49
C III 977	SF, $M_* \leq 10^{10.5} M_\odot$	834	440	567	806 ± 226	403 ± 247	576 ± 306	14.6	14.1	14.3	14.5 ± 0.13	14.0 ± 0.33	14.2 ± 0.38
C III 977	SF, $M_* \geq 10^{10.5} M_\odot$	605	446	555	643 ± 176	252 ± 275	531 ± 264	14.3	14.1	14.3	14.4 ± 0.18	13.8 ± 0.70	14.1 ± 0.50
Si III 1206	All	322	130	193	398 ± 281	207 ± 173	286 ± 241	13.5	12.9	13.0	13.4 ± 0.48	13.0 ± 0.46	13.1 ± 0.50
Si III 1206	sSFR < 10 <sup>-11</sup> yr <sup>-1</sup>	169	340	169	196 ± 209	281 ± 232	257 ± 221	13.0	13.4	13.0	12.9 ± 0.54	13.1 ± 0.62	13.0 ± 0.58
Si III 1206	sSFR ≥ 10 <sup>-11</sup> yr <sup>-1</sup>	409	130	233	460 ± 277	155 ± 91	302 ± 253	13.5	12.9	13.2	13.5 ± 0.39	12.9 ± 0.31	13.2 ± 0.46
Si III 1206	$M_* < 10^{10.5} M_\odot$	259	107	139	410 ± 307	121 ± 62	265 ± 261	13.3	12.8	13.0	13.4 ± 0.54	12.8 ± 0.24	13.1 ± 0.50
Si III 1206	$M_* \geq 10^{10.5} M_\odot$	409	233	281	385 ± 270	259 ± 198	303 ± 228	13.5	13.3	13.3	13.4 ± 0.44	13.1 ± 0.52	13.2 ± 0.50
Si III 1206	SF, $M_* \leq 10^{10.5} M_\odot$	564	107	139	455 ± 295	121 ± 62	278 ± 264	13.7	12.8	13.0	13.5 ± 0.43	12.8 ± 0.24	13.1 ± 0.49
Si III 1206	SF, $M_* \geq 10^{10.5} M_\odot$	409	233	322	470 ± 280	215 ± 110	342 ± 241	13.5	13.3	13.4	13.5 ± 0.35	13.1 ± 0.31	13.3 ± 0.38

**Notes.** Median and average values for equivalent width and column density of selected metal-line transitions as a function of impact parameter in kpc. In all estimations, lower and upper limits are taken at their respective values.

<sup>a</sup>  $\tilde{W}$  is the median equivalent width for the given transition, in mÅ.

<sup>b</sup>  $\langle W \rangle$  gives the average and rms of the equivalent width values, in mÅ.

<sup>c</sup>  $\log \tilde{N}$  is the median column density measured from all observed transitions of the given ion.

<sup>d</sup>  $\langle \log N \rangle$  gives the average and rms of the logarithmic column densities.

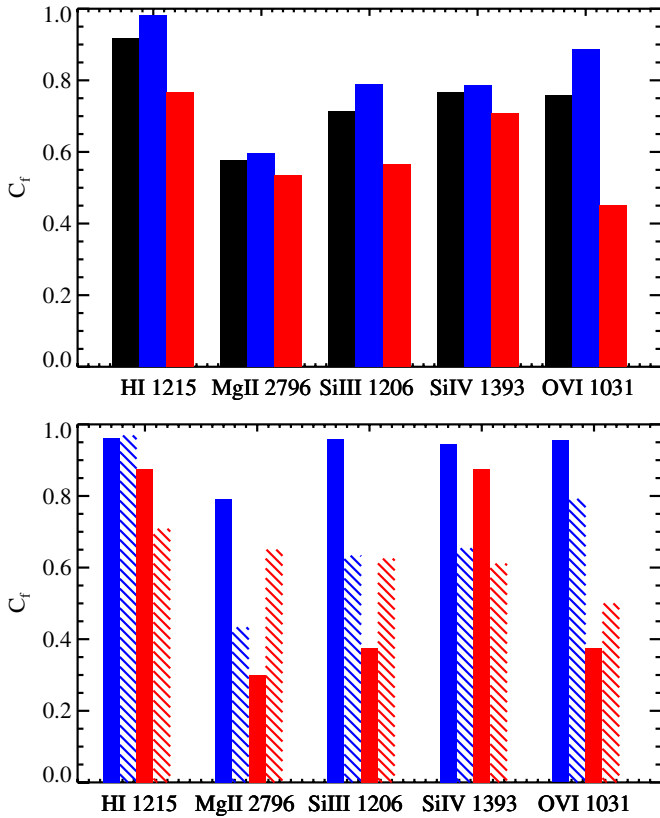


**Figure 12.** Upper: covering fraction  $C_f$  of ionic absorption (equivalent widths) for the COS-Halos sample of galaxies, as measured to  $R = 160$  kpc (Table 5). The black/blue/red bars indicate the full/SF/non-SF samples, respectively. The high incidence of H I gas requires a cool CGM surrounding  $L^*$  galaxies (J. Tumlinson et al., in preparation), and the significant  $C_f$  values for the various metal-line transitions implies a metal-enriched gas. Within the metal-line transitions, one notes that  $C_f$  rises with increasing ionization state, especially for the SF population. Lower: covering fraction  $C_f$  of ionic absorption (equivalent widths) separated by impact parameter: solid bars refer to  $R < 75$  kpc and hashed are for  $R \geq 75$  kpc. Within the SF population (blue), there is a clear difference between the two radial cuts, aside from H I absorption. This suggests declining metal enrichment with increasing  $R$ , which we will explore in a future paper (J. K. Werk et al., in preparation). Oddly, the opposite trend is noted for the quiescent galaxies (red). We are concerned, however, that this is driven by small sample size of this sub-population.

(A color version of this figure is available in the online journal.)

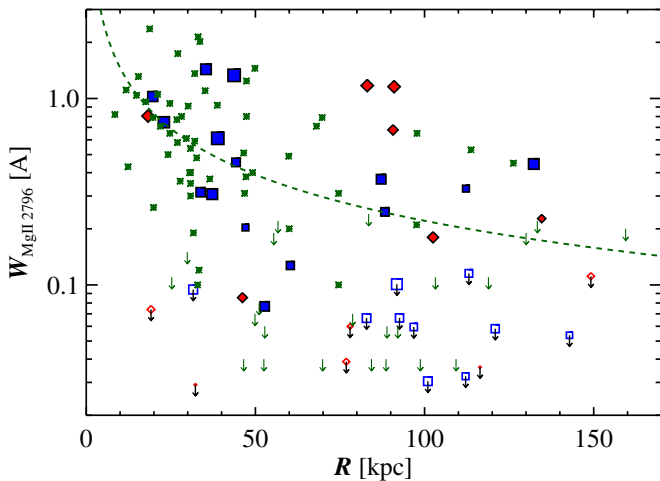


**Figure 13.** Equivalent width of the MgII  $\lambda 2796$  line as a function of impact parameter for the COS-Halos data (red and blue points) and comparing to the data published by Chen et al. (2010, green asterisks and arrows). We also show the fit to the data from Chen et al. (2010).

(A color version of this figure is available in the online journal.)

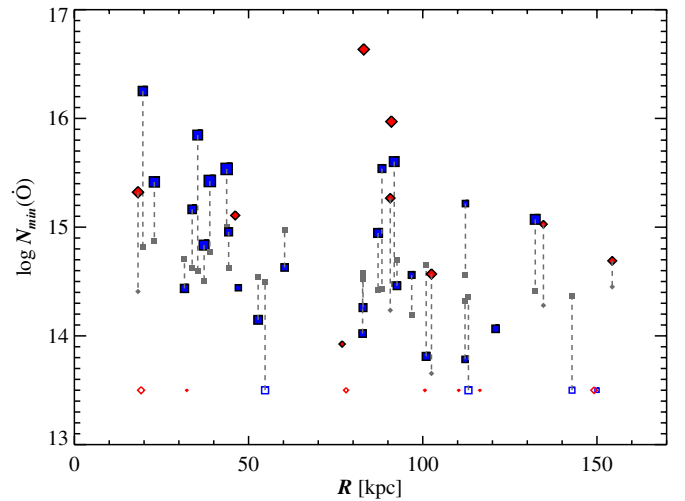


**Figure 14.**  $N_{\text{min}}(\text{O})$ , the minimum metal column density in the cool phase of the CGM ( $T < 10^5$  K) described in Section 5, vs. impact parameter. The gray points connected to this quantity by gray dashed lines show the values of  $\log N_{\text{O}^+5}$  published by Tumlinson et al. (2011) for comparison. In cases where we do not detect gas in this low-ionization state cool phase, we plot open symbols with  $N_{\text{min}}(\text{O}) = 10^{13.5} \text{ cm}^{-2}$ . The symbol sizes correspond to  $N_{\text{H I}}$ , where bigger color symbols have larger  $N_{\text{H I}}$ .

(A color version of this figure is available in the online journal.)

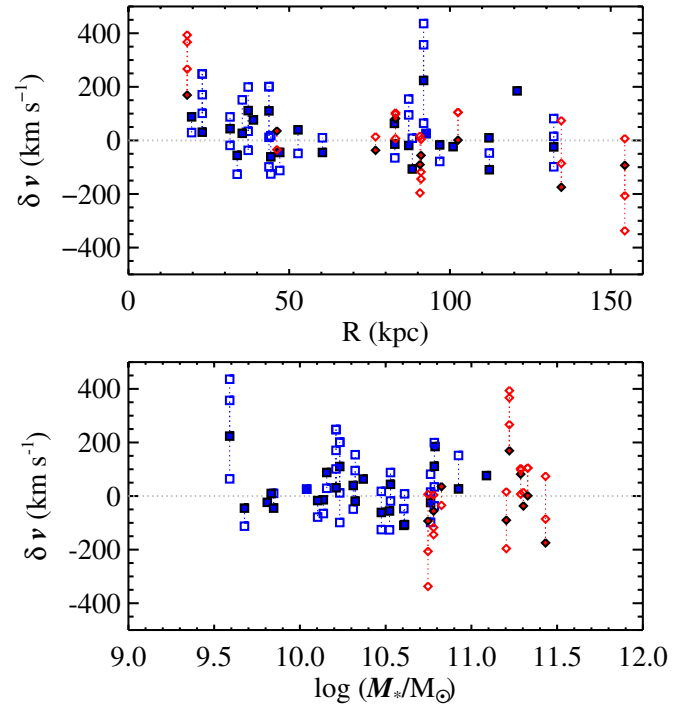


**Figure 15.** Fitted component centroid velocities with respect to galaxy systemic redshift,  $\delta v$ , as a function of impact parameter and stellar mass for the low and intermediate ionization state metal lines examined in this work (one of MgII, CII, CIII, SiIII). The dotted lines span the full range in velocity over which the transition is defined. The dominant component is shown as a solid point (blue squares denote SF galaxies; red diamonds denote quiescent galaxies), while other fitted components are shown as open symbols. The majority of the gas is bound to the dark matter halo:  $v_{\text{esc}}$  at  $R = 150$  kpc for an  $L^*$  galaxy is  $\approx 200 \text{ km s}^{-1}$ .

(A color version of this figure is available in the online journal.)

These measurements are derived from far-UV transitions observed in *HST*/COS and Keck/HIRES spectra of background quasars within an impact parameter  $R < 160$  kpc to the targeted galaxies at  $z \sim 0.2$ . We have closely examined empirical

relations between the CGM and galaxy properties. Additionally, we have analyzed adjacent ionization states of different species and compared the kinematic structure of their individual fitted components. Here, we summarize our main findings on the qualitative nature of the  $z \sim 0$  CGM as described by our new observations.

1. Low and intermediate ionization state metal absorption lines are a very common feature of the CGM for  $L^*$  galaxies of all spectral types (33/44 galaxies show absorption from low/intermediate ionization state material). This frequent presence of substantial lower ionization state material (e.g.,  $\text{Mg}^+$ ,  $\text{Si}^+$ ,  $\text{Si}^{++}$ ,  $\text{C}^{++}$ ) requires a cool component for the CGM ( $T < 10^5$  K), consistent with our results on the H I gas (J. Tumlinson et al., in preparation; Thom et al. 2012).
2. A comparison of the relative column densities of adjacent ionization states of low and intermediate ions indicates that the gas is predominantly ionized.
3. The detection rates and column densities derived for the low and intermediate ionization state metal lines decrease with increasing impact parameter, a trend we interpret as a declining metal surface density profile for the CGM within its inner 160 kpc.
4. There is large dispersion in low and intermediate ion absorption strengths, independent of galaxy properties. This variation implies a patchy distribution of dense, cool CGM gas.
5. The qualitative comparison of the absorption-line profiles between low and intermediate ions indicates an overall correspondence of component structure and shape. We find no evidence that the low and intermediate ionization states of the cool CGM arise from distinct phases. However, an additional comparison of these profiles with those of  $\text{O}^{+5}$ , as analyzed by Tumlinson et al. (2011), suggests a complex relationship between low/intermediate ionization states and more highly ionized gas that will be fully explored in future work.
6. The gas kinematics derived from Voigt profile fits to the data suggest the CGM is largely bound to its host galaxy's dark matter halo. Furthermore, the frequent presence of multiple velocity components indicate the material is clumpy.
7. The metal column densities of the low and intermediate ionization state gas imply that the CGM is a massive gaseous reservoir, its baryonic content estimated to far exceed  $10^9 M_\odot$  based on conservative assumptions. This mass estimate was made independently of the mass estimate discussed by Tumlinson et al. (2011), which was based on  $\text{O}^{+5}$  measurements alone. The cool ( $T < 10^5$  K) and warm ( $T \approx 10^5\text{--}10^6$  K)  $\text{O}^{+5}$ -traced CGM may represent completely distinct gas phases whose total masses will contribute separately to the CGM baryonic content. An upcoming paper (J. K. Werk et al., in preparation) will report a full analysis of the ionized gas fraction and metallicity of the gas using photoionization modeling, and will provide a more reliable baryonic mass estimate for the cool CGM of  $z \sim 0L^*$  galaxies.

Support for program GO11598 was provided by NASA through a grant from the Space Telescope Science Institute, which is operated by the Association of Universities for Research in Astronomy, Inc., under NASA contract NAS 5-26555. Much of the data presented herein were obtained at the W. M. Keck Observatory, which is operated as a scientific partnership among the California Institute of Technology, the University of

California, and the National Aeronautics and Space Administration. The Observatory was made possible by the generous financial support of the W. M. Keck Foundation. The authors wish to recognize and acknowledge the very significant cultural role and reverence that the summit of Mauna Kea has always had within the indigenous Hawaiian community. We are most fortunate to have the opportunity to conduct observations from this mountain. J.X.P. acknowledges support from a Humboldt visitor fellowship to the Max Planck Institute for Astronomy, where part of this work was performed. J.K.W. thanks the referee of this work, John Stocke, for very helpful comments that improved the manuscript.

*Facilities:* Keck:I (HIRES), HST (COS)

## REFERENCES

- Aracil, B., Tripp, T. M., Bowen, D. V., et al. 2006, *MNRAS*, **367**, 139
- Asplund, M., Grevesse, N., & Sauval, A. J. 2005, in ASP Conf. Ser. 336, *Cosmic Abundances as Records of Stellar Evolution and Nucleosynthesis*, ed. T. G. Barnes & F. N. Bash (San Francisco, CA: ASP), 25
- Bahcall, J. N., & Spitzer, L. J. 1969, *ApJL*, **156**, 63
- Barton, E. J., & Cooke, J. 2009, *AJ*, **138**, 1817
- Bergeron, J. 1986, *A&A*, **155**, L8
- Blanton, M. R., Hogg, D. W., Bahcall, N. A., et al. 2003, *ApJ*, **592**, 819
- Blanton, M. R., & Roweis, S. 2007, *AJ*, **133**, 734
- Bowen, D. V., Blades, J. C., & Pettini, M. 1995, *ApJ*, **448**, 634
- Bowen, D. V., & Chelouche, D. 2011, *ApJ*, **727**, 47
- Bowen, D. V., Pettini, M., & Blades, J. C. 2002, *ApJ*, **580**, 169
- Chen, H., Helsby, J. E., Gauthier, J., et al. 2010, *ApJ*, **714**, 1521
- Chen, H., Lanzetta, K. M., Webb, J. K., & Barcons, X. 1998, *ApJ*, **498**, 77
- Chen, H.-W., Lanzetta, K. M., & Webb, J. K. 2001, *ApJ*, **556**, 158
- Cooksey, K. L., Thom, C., Prochaska, J. X., & Chen, H. 2010, *ApJ*, **708**, 868
- Davé, R., & Tripp, T. M. 2001, *ApJ*, **553**, 528
- Dunkley, J., Komatsu, E., Nolte, M. R., et al. 2009, *ApJS*, **180**, 306
- Feigelson, E. D., & Nelson, P. I. 1985, *ApJ*, **293**, 192
- Froning, C. S., & Green, J. C. 2009, *Ap&SS*, **320**, 181
- Ghavarni, P., Aloisi, A., Lennon, D., et al. 2009, Preliminary Characterization of the Post-launch Line Spread Function of COS, Technical Report
- Gnat, O., & Sternberg, A. 2007, *ApJS*, **168**, 213
- Green, J. C., Froning, C. S., Osterman, S., et al. 2012, *ApJ*, **744**, 60
- Kacprzak, G. G., Churchill, C. W., Ceverino, D., et al. 2010, *ApJ*, **711**, 533
- Kartaltepe, J. S., Sanders, D. B., Scoville, N. Z., et al. 2007, *ApJS*, **172**, 320
- Koester, B. P., McKay, T. A., Annis, J., et al. 2007, *ApJ*, **660**, 239
- Lanzetta, K. M., Bowen, D. V., Tytler, D., & Webb, J. K. 1995, *ApJ*, **442**, 538
- Lin, L., Koo, D. C., Willmer, C. N. A., et al. 2004, *ApJL*, **617**, 9
- Ménard, B., & Chelouche, D. 2009, *MNRAS*, **393**, 808
- Morris, S. L., Weymann, R. J., Dressler, A., et al. 1993, *ApJ*, **419**, 524
- Morton, D. C. 2003, *ApJS*, **149**, 205
- Mulchaey, J. S., & Chen, H.-W. 2009, *ApJL*, **698**, 46
- Okamoto, T., & Habe, A. 1999, *ApJ*, **516**, 591
- Penton, S. V., Shull, J. M., & Stocke, J. T. 2000, *ApJ*, **544**, 150
- Penton, S. V., Stocke, J. T., & Shull, J. M. 2002, *ApJ*, **565**, 720
- Prochaska, J. X., Chen, H.-W., Howk, J. C., Weiner, B. J., & Mulchaey, J. 2004, *ApJ*, **617**, 718
- Prochaska, J. X., Weiner, B., Chen, H.-W., Cooksey, K. L., & Mulchaey, J. S. 2011a, *ApJS*, **193**, 28
- Prochaska, J. X., Weiner, B., Chen, H.-W., Mulchaey, J., & Cooksey, K. 2011b, *ApJ*, **740**, 91
- Ribaudo, J., Lehner, N., Howk, J. C., et al. 2011, *ApJ*, **743**, 207
- Rudie, G. C., Steidel, C. C., Trainor, R. F., et al. 2012, *ApJ*, **750**, 67
- Savage, B. D., & Sembach, K. R. 1996, *ARA&A*, **34**, 279
- Savage, B. D., Tripp, T. M., & Lu, L. 1998, *AJ*, **115**, 436
- Shull, J. M., Stocke, J. T., & Penton, S. 1996, *AJ*, **111**, 72
- Steidel, C. C., Kollmeier, J. A., Shapley, A. E., et al. 2002, *ApJ*, **570**, 526
- Stewart, K. R., Kaufmann, T., Bullock, J. S., et al. 2011, *ApJ*, **738**, 39
- Stocke, J. T., Penton, S. V., Danforth, C. W., et al. 2006, *ApJ*, **641**, 217
- Stocke, J. T., Shull, J. M., Penton, S., Donahue, M., & Carilli, C. 1995, *ApJ*, **451**, 24
- Thom, C., & Chen, H. 2008a, *ApJS*, **179**, 37
- Thom, C., & Chen, H. 2008b, *ApJ*, **683**, 22
- Thom, C., Tumlinson, J., Werk, J., Prochaska, J. X., & Tripp, T. 2012, *ApJ*, **758**, 41

- Tilton, E. M., Danforth, C. W., Shull, J. M., & Ross, T. L. 2012, [ApJ](#), **759**, 112
- Tripp, T. M., Giroux, M. L., Stocke, J. T., Tumlinson, J., & Oegerle, W. R. 2001, [ApJ](#), **563**, 724
- Tripp, T. M., Lu, L., & Savage, B. D. 1998, [ApJ](#), **508**, 200
- Tripp, T. M., Meiring, J. D., Prochaska, J. X., et al. 2011, [Sci](#), **334**, 952
- Tripp, T. M., & Savage, B. D. 2000, [ApJ](#), **542**, 42
- Tripp, T. M., Sembach, K. R., Bowen, D. V., et al. 2008, [ApJS](#), **177**, 39
- Tumlinson, J., & Fang, T. 2005, [ApJL](#), **623**, 97
- Tumlinson, J., Thom, C., Werk, J. K., et al. 2011, [Sci](#), **334**, 948
- Wakker, B. P., & Savage, B. D. 2009, [ApJS](#), **182**, 378
- Werk, J. K., Prochaska, J. X., Thom, C., et al. 2012, [ApJS](#), **198**, 3
- Zepf, S. E., & Koo, D. C. 1989, [ApJ](#), **337**, 34